



1 **Characteristics of ozone and particles in the near-surface**
2 **atmosphere in urban area of the Yangtze River Delta, China**

3 Huimin Chen¹, Bingliang Zhuang^{1,*}, Jane Liu^{1,2}, Tijian Wang^{1,**}, Shu Li¹, Min Xie¹, Mengmeng
4 Li¹, Pulong Chen¹, Ming Zhao¹

5 ¹School of Atmospheric Sciences, CMA-NJU Joint Laboratory for Climate Prediction Studies,
6 Jiangsu Collaborative Innovation Center for Climate Change, Nanjing University, Nanjing 210023,
7 China

8 ²Department of Geography and Planning, University of Toronto, Toronto, M5S 3G3, Canada

9 Correspondence: Bingliang Zhuang (blzhuang@nju.edu.cn) and Tijian Wang
10 (tiwang@nju.edu.cn)

11 **Abstract**

12 To improve the understanding of the interactions between particles and trace gases in a typical city
13 of the YRD region, continuous measurements of particles and trace gases were made at an urban
14 site in Nanjing during cold seasons in 2016 in this study. The average of particles, including black
15 carbon (BC), PM_{2.5}, and PM₁₀ are $2.602 \pm 1.720 \mu\text{g}/\text{m}^3$, $58.2 \pm 36.8 \mu\text{g}/\text{m}^3$, and $86.3 \pm 50.8 \mu\text{g}/\text{m}^3$,
16 respectively, while the average of trace gases, which contain CO, O₃, NO_x, and NO_y, are $850.9 \pm$
17 384.1 , 37.7 ± 33.5 , 23.5 ± 14.7 , and 32.8 ± 22.3 ppb, respectively. Compared to National Ambient
18 Air Quality Standards in China (NAAQS-CN), we found 48 days excess of PM_{2.5}, 14 days excess
19 of PM₁₀, and 40 days excess of O₃. The particles, CO, and nitrogen oxide concentrations shared a
20 similar pattern of seasonality and diurnal cycles, which are different from O₃. The former ones are
21 all high in DJF and at rush hours, while the latter one had high loadings in the daytime, especially



22 when the ultra violet (UV) was high. Correlation analysis reveals the formation of secondary
23 aerosols, especially $PM_{2.5}$, under high O_3 and temperature conditions, and suggests a
24 VOC-sensitive regime for photochemical production of O_3 in urban Nanjing in cold seasons.
25 Backward trajectory analysis suggests the prevailing winds in Nanjing were northerly and easterly
26 during cold seasons in 2016. Air masses from eastern without passing through the urban
27 agglomeration and those from northern without crossing BTH regions were cleaner, but air masses
28 from local regions were more polluted in winter. A case study for a typical O_3 and $PM_{2.5}$ episode
29 in December 2016 demonstrated that the episode was generally associated with regional transport
30 and stable weather system. Air pollutants were mostly transported from the western areas with
31 high emissions and weather conditions are controlled by anticyclone and high-pressure system in
32 this region. This study further reveals the important effects of weather system and human activities
33 on the environment in the YRD region, especially in the urban areas, and it's an urgent need for
34 improving air quality in these areas.

35

36 **1. Introduction**

37 Particles, including black carbon (BC), $PM_{2.5}$, and PM_{10} , and trace gases, such as
38 carbon monoxide (CO), ozone (O_3), nitric oxide and nitrogen dioxide (NO_x), and total
39 reactive nitrogen (NO_y), are important components in the troposphere because of their
40 impacts on human health, biosphere and climate changes (e.g., Chameides et al.,
41 1999a, b; Jerrett et al., 2009; Allen et al., 2012). BC is mostly from incomplete
42 combustion of coal, diesel fuels, biofuels, and outdoor biomass burning (Bond et al.,



43 2004). Although BC accounts for a relatively small portion of the total mass
44 concentrations of aerosol particles in atmosphere, it plays a significant role in global
45 radiation balance, both directly and indirectly. Thus, BC could influence the global
46 and region climate changes and atmospheric environment substantially (Jacobson et
47 al., 2002; Bond et al., 2013; Deng et al., 2010). Particulate matters (PMs) originate
48 from both natural and anthropogenic emission sources (Kaufman et al., 2002). Due to
49 prosperous economic development, rapid industrialization and urbanization in recent
50 decades, haze events have frequently occurred in the Beijing-Tianjin-Hebei (BTH)
51 area, Yangtze River Delta (YRD) and Pearl River Delta (PRD) regions, all of which
52 were mainly caused by high concentrations of particulate matter. Tropospheric ozone
53 is a typical secondary air pollutant that is related to its precursors NO_x and VOCs
54 (Crutzen, 1973) through several complicated reactions. O₃ could impact tropospheric
55 environment (Monks et al., 2015), and make significant contributions to radiative
56 forcing of climate (Intergovernmental Panel on Climate Change (IPCC), 2007).
57 Tropospheric O₃ precursors and the interactions between O₃ and its precursors in
58 different geographical locations are usually different, and thereby the
59 characterizations of O₃ at different sites can vary greatly (Xie et al., 2016). The impact
60 of PMs and BC on surface ozone is a topic that has attracted much attention. Jacobson
61 (1998) reported that aerosols containing BC cores reduced photolysis rates and
62 resulted in a decrease in ozone concentrations by 5%–8% at ground level in Los
63 Angeles. It is also found that a strong reduction in photolysis rate (10%–30%) due to
64 BC-containing aerosols (Castro et al., 2001) led to a decrease in surface ozone in



65 Mexico City. Similar results have been found in other studies simulating the effects of
66 BC on surface ozone in China (Li et al., 2011).
67 Most of earlier studies on particles were focused on concentrations estimation, the
68 chemical characteristics, potential sources, as well as climate effects of particulate
69 matters based on numerical simulations (Wu et al., 2012; Song et al., 2014; Xiao et al.,
70 2012; Yu et al., 2015; Kristjánsson, 2002; Liao and Seinfeld, 2005; Zhuang et al.,
71 2010; 2013), while observation-based studies of particles were relatively limited. In
72 addition, although a good understanding of the characteristics of O₃ have been gained
73 in the BTH area and the PRD region (Wang et al., 2009; Zheng et al., 2010; Lin et al., 2008)
74 due to a relatively long history of research limited in the megacities, in the YRD
75 region, there were only very limited studies of O₃ made in urban areas in some YRD
76 cities (Tu et al., 2007; Ding et al., 2013; Xie et al., 2016), most of which were based
77 on studies of O₃ measurement beginning in the 1990s at Lin'an site, a rural region in
78 the southeast YRD (Luo et al., 2000). And most of studies in YRD on particles, or
79 particulate matter, were done in the eastern YRD, close to Shanghai, and mainly
80 covered short periods of time. In the YRD region, the prevailing winds are from
81 between the northeast and southeast. Therefore, western YRD region is under a
82 downwind condition. As only few measurement studies have been conducted for
83 western YRD (Tu et al., 2007), large knowledge gaps still exist in our understanding
84 of the characteristics and main sources of O₃ and particles (Ding et al., 2013) in the
85 region, let alone their interactions.

86



87 China is always one of the major source regions of particles. Over recent decades,
88 along with the rapid economic development and the growing demand of energy
89 consumption, many areas in China are suffering from the elevated O₃ pollution. In the
90 BTH area, the YRD region, and the PRD region, all of which are the economically
91 vibrant and densely populated, high levels of ozone precursor emissions and O₃
92 pollution have become one of the major environment problems affecting the public
93 (Chan and Yao, 2008; Zhang et al., 2009; Ma et al., 2012; Xie et al., 2016). Because
94 of complex sources and chemical reactions, and relatively long atmospheric lifetimes
95 of the pollutants in the atmosphere that favors regional and long-range transport, all
96 the pollutants are of great concern for regional air quality but are very difficult to
97 control (Cooper et al., 2005; Zhang et al., 2008). The YRD is located in the eastern
98 part of the Yangtze River Plain, adjacent to the most polluted North China Plain,
99 including large cities of Shanghai, southern Jiangsu and northern Zhejiang. Taking up
100 only 2 percent of the land area in China, this region produces over 20 percent of
101 China's Gross Domestic Product (GDP). Nanjing, as the capital of Jiangsu Province,
102 lies in the middle of YRD. It covers an area over 6000 km², with more than 7.3
103 million residents (<http://www.njtj.gov.cn/>). Being the second largest commercial
104 center after Shanghai in YRD, even the East China, Nanjing is highly urbanized and
105 industrialized. Both particles and O₃ concentrations are found to be high in Nanjing,
106 which affects regional climate and air quality (Zhang et al., 2009; Yi et al., 2015).
107 Therefore, the issue of air pollution in Nanjing deserves attentions. In this study,
108 continuous observations of particles, trace gases and certain aerosol optical properties



109 at an urban station in Nanjing (a typical developing city in YRD) have been made in
110 order to characterize the air pollution in the city. In the following, we describe the
111 methodology in Section 2. Results and discussions are presented in Section 3,
112 followed by Conclusions in Section 4.

113 **2. Methodology**

114 **2.1 Brief Introduction to the Urban Atmospheric Observational Station**

115 The Urban Atmospheric Observational Station is a regional atmospheric urban station
116 located on the Gulou Campus of Nanjing University in the downtown area of Nanjing
117 (32.05 °N, 118.78 °E), and run by School of Atmospheric Sciences, Nanjing
118 University. It is built on the roof of a 79.3m tall building, without any industrial
119 pollution sources within a 30 km radius around but several main roads with evident
120 traffic pollution, especially during rush hours. The sketch map of the site (not shown)
121 and the corresponding climatology have been described in Zhu et al (2012).

122

123 The Particles, O₃, NO_x, NO_y, CO, and wavelength-dependent aerosol optical
124 parameters including aerosol scattering (SC), back-scattering (Bsp), and absorption
125 (AAC) coefficients have been routinely measured at the station during the time period
126 from 1 Sep 2016 to 28 Feb 2017. The AAC and concentrations of BC were derived
127 from the measurements using a seven-channel Aethalometer (model AE-31, Magee
128 Scientific, USA). The aerosol SC and Bsp were measured with a



129 three-wavelength-integrating Nephelometer (Aurora 3000, Australia). The AE-31
130 model measures light attenuation at seven wavelengths, including 370, 470, 520, 590,
131 660, 880 and 950 nm, with a desired flow rate of 5.0 L min⁻¹ and a sampling interval
132 of 5 min. Aurora 3000 measures aerosol light scattering, including SC and Bsp at 450,
133 525 and 635 nm, with a sampling interval of 1 min (Zhuang et al. 2017). Precision
134 and instrument of the measurements in this study are listed in Table 1.

135

136 Monthly averaged meteorological parameters during the period from Sep.2016 to
137 Feb.2017 at the station are shown in Table 2. The air temperature at the site ranged
138 from 6.64°C in Feb.2017 to 24.88°C in Sep.2016. The relative humidity (RH) was
139 higher in fall than in winter, especially in October, while the precipitation was heavier
140 in fall than in winter. Visibility (Vis) varied in different months. The peak of the
141 ultraviolet radiation (UV) occurred in Sep.2016, after which the radiation became
142 weak till the end of Jan.2017, and rose a little in Feb.2017.

143

144 **2.2 Calculation of the aerosol optical properties**

145 The wavelength-dependent AAC, which is associated with the intensities of the
146 incoming light and remaining light after passing through a medium, can be calculated
147 directly using the measured light attenuations (ATN) through a quartz filter matrix, a
148 percentage to represent the filter attenuation, as well as BC mass concentrations
149 (Petzold et al., 1997; Weingartner et al., 2003; Arnott et al., 2005; Schmid et al.,



150 2006):

$$151 \quad \sigma_{ATN, t(\lambda)} = \frac{(ATN_t(\lambda) - ATN_{t-1}(\lambda))}{\Delta t} \times \frac{A}{V}, \quad (1)$$

152 where A (in m^2) is the area of the aerosol-laden filter spot, V is the volumetric
153 sampling flow rate (in L min^{-1}) and Δt is the time interval (=5 min) between t and
154 $t-1$. σ_{ATN} , known as AAC without any correction, is larger than the actual aerosol
155 absorption coefficient σ_{abs} in general. The key factors leading to the bias are as
156 follows: (1). multiple-scattering of light at the filter fibers (multiple-scattering effect),
157 and (2) the instrumental response with increased particle loading on the filter
158 (shadowing effect). The former results in the overestimation of the σ , while the later
159 causes underestimation of the σ . Thus, the correction is needed and the calibration
160 factors C and R (shown in Eq. 2) are introduced against the scattering effect and
161 shadowing effect, respectively:

$$162 \quad \sigma_{\text{abs}, t(\lambda)} = \frac{\sigma_{ATN, t(\lambda)}}{C \times R}. \quad (2)$$

163 Weingartner (Weingartner et al., 2003, WC2003 for short, hereinafter), Arnott (Arnott
164 et al., 2005), Schmid (Schmid et al., 2006, SC2006 for short, hereinafte), and Virkkula
165 (Virkkula et al., 2007) corrections, have been developed to eliminate the uncertainties.
166 Zhuang et al. (2015) further suggested that wavelength-dependent AACs corrected by
167 SC2006 might be closer to the real ones than WC2003s in Nanjing, although 532 nm
168 AACs from these two corrections are close to each other.

169 Therefore, AACs corrected from SC2006 are used in this study.

170



171 Measurement of Aurora 3000, a nephelometer with newly designed light sources
172 based on light emitting diodes, needs correction using Mie-theory for measurement
173 artefacts. Müller et al. (2011) provided parameterizations for the angular sensitivity
174 functions of Aurora 3000, which follows the definition of correction factors from
175 Anderson and Ogren (1998), where the ratios of true to measured nephelometer
176 values for both total scattering and backscattering are defined by:

$$177 \quad C_{ts,\lambda} = \frac{\sigma_{ts,\lambda}^{true} \sigma_{tsR,\lambda}^{neph}}{\sigma_{ts,\lambda}^{neph} \sigma_{tsR,\lambda}^{true}}, \quad (4)$$

178 and

$$179 \quad C_{bs,\lambda} = \frac{\sigma_{bs,\lambda}^{true} \sigma_{bsR,\lambda}^{neph}}{\sigma_{bs,\lambda}^{neph} \sigma_{bsR,\lambda}^{true}}, \quad (5)$$

180 where σ_{ts}^{true} and σ_{bs}^{true} are true total scattering coefficient and backscattering
181 coefficient for ideal angular sensitivity functions, respectively, $\sigma_{tsR,\lambda}$ and $\sigma_{bsR,\lambda}$ are
182 Rayleigh total scattering coefficient and backscattering coefficient, respectively, and
183 σ_{ts}^{neph} and σ_{bs}^{neph} are nephelometer total scattering coefficient and backscattering
184 coefficient, respectively. In this study, we assume that Rayleigh scattering is
185 equivalent to true scattering.

186

187 The correction factors can be calculated using measured size distributions or SAE.
188 Anderson and Ogren (1998), hereinafter denoted as AO98, found a dependency
189 between the SAE and the correction factor for total scattering. The correction was
190 given by:

$$191 \quad C_{ts} = a + b \cdot a_{ts}^* \quad (6)$$



192 where α_{sc}^* is the scattering Ångström exponent derived from uncorrected nephelometer
193 scattering. According to Müller et al. (2011), for backscattering, there was no
194 correlation between correction factors and scattering Ångström exponents, which is in
195 agreement with AO98. The parameters a and b were derived from Mie calculated
196 true scattering and simulated nephelometer scattering for ranges of particle sizes and
197 refractive indices.

198

199 In this study, we used the correction factors for Aurora 3000 without a sub- μm cut in
200 Müller et al. (2011), which are shown in the Table 3. According to nephelometer
201 correction factors for angular nonidealities, which are shown in Table 3(a), original
202 scattering coefficient (SC at 635 nm, 525 nm and 450 nm) and backscattering
203 coefficient (Bsp at 635 nm, 525 nm and 450 nm) obtained from the measurements are
204 corrected based on Eqs (4) and Eqs (5). We also calculated correction factors for total
205 scatter as function of Ångström exponent shown in Table 3.(b), original scattering
206 coefficient (SC at 635 nm, 525 nm and 450 nm) are corrected based on Eqs (6).

207

208 Based on corrected wavelength-dependent AAC and SC, SAE and AAE are estimated
209 by the following:

$$210 \quad AAE_{470 / 660\text{nm}} = -\log(AAC_{470\text{nm}} / AAC_{660\text{nm}}) / \log(470 / 660), \quad (7)$$

$$211 \quad SAE_{450 / 635\text{nm}} = -\log(SC_{450\text{nm}} / SC_{635\text{nm}}) / \log(450 / 635), \quad (8)$$

$$212 \quad \sigma_{\lambda} = \sigma_{\lambda_0} \times \left(\frac{\lambda}{\lambda_0}\right)^{-\alpha}, \quad (9)$$



213 where σ_λ is the coefficient at wavelength λ and α is the corresponding Ångström
214 exponents.

215

216 On the basis of Eqs (7) ~Eqs (9), SC and Bsp at 550 nm were calculated for
217 comparison. Between the two ways of corrections, the results of the total scattering
218 coefficients are in agreement with each other in general, with differences of 10.67%.

219 In this study, we choose the results from the correction using SAE.

220 Meanwhile, based on wavelength-dependent SC, Bsp, AAC, aerosol asymmetry
221 parameter (ASP), single-scattering albedo (SSA) and extinction coefficient (EC) are
222 further estimated:

$$223 \quad ASP_\lambda = -7.143889\beta_\lambda^3 + 7.46443\beta_\lambda^2 - 3.9356\beta_\lambda + 0.9893, \quad (10)$$

$$224 \quad SSA_\lambda = \frac{SC_\lambda}{SC_\lambda + AAC_\lambda}, \quad (11)$$

$$225 \quad EC_\lambda = SC_\lambda + AAC_\lambda, \quad (12)$$

226 where is β_λ the ratio of Bsp to SC at wavelength λ . Equation (10) is derived from

227 Andrews et al. (2006).

228 Table 4 shows the statistical summary of the surface aerosol optical properties in
229 Nanjing after the correction. The mean value during the cold seasons in 2016 of AAC,
230 SC, Bsp, EC, SSA and ASP at 550 nm, AAE at 470/660 nm and SAE at 450/635 nm
231 are 23.741, 349.502, 35.469, 373.536 Mm^{-1} , 0.929, 0.645, 1.600, and 1.192, with a
232 standard deviation of 15.556, 235.291, 21.488, 247.877 Mm^{-1} , 0.028, 0.052, 0.175,
233 and 0.288, respectively.

234



235 2.3 HYSPLIT model

236 In order to understand the general transport characteristics of air masses recorded at
237 this station, we conducted a 4 d (96 h) backward trajectory simulations during the
238 cold seasons in 2016 using a Lagrangian dispersion model Hybrid Single-Particle
239 Lagrangian Integrated Trajectory (HYSPLIT) (version 4.9) provided by the Air
240 Resource Laboratory (ARL) of the USA National Oceanic and Atmospheric
241 Administration (NOAA) (Draxler and Hess, 1998). HYSPLIT - 4 Model is capable of
242 processing multiple gas input fields, multiple physical processes and different types of
243 pollutant emission sources and has been widely used in the study of transport and
244 diffusion of various pollutants in various regions (Mcgowan and Clark, 2008; Wang
245 et al., 2011; Wang et al., 2015). It is one of the most extensively used atmospheric
246 transport and dispersion models for the study of air parcel trajectories (Draxler and
247 Rolph, 2013; Stein et al., 2016). In this study, backward trajectories were calculated
248 and clustered using a stand-alone version of the NCEP / NCAR reanalyzed
249 meteorological field (<http://ready.arl.noaa.gov/archives.php>). The NCEP data contain
250 6-hourly basic meteorological fields on pressure surfaces, with the spatial resolution
251 of 2.5°, corresponding to the 00, 06, 12, 18 UTC, respectively. In this study, the data
252 are also converted to hemispheric 144 by 73 polar stereographic grids, which is the
253 same grid configuration as the dataset applied in synoptic weather classification. For
254 each synoptic weather pattern, the backward trajectories were started at Gulou station
255 in Nanjing (32°N, 118.8°E).



256 3. Results and discussion

257 3.1 Characteristics of particulate matter in Nanjing

258 The hourly-mean concentrations of particles at Gulou site during the cold seasons in
259 2016 are shown in Fig 1. Gaps in the time series are missing values. The averaged
260 values of BC, PM_{2.5} and PM₁₀ during the study period are 2.6 ± 1.7 , 58.2 ± 36.8 , and
261 $86.3 \pm 50.8 \mu\text{g}/\text{m}^3$, respectively. The average of particulate matter concentrations
262 during the study period are higher than standard concentrations, which are $35 \mu\text{g}/\text{m}^3$
263 for fine and $70 \mu\text{g}/\text{m}^3$ for PM₁₀. Particles, including BC, PM_{2.5} and PM₁₀ fluctuate
264 similarly, because the three particulates originate mostly from the same sources, i.e.,
265 transport emissions. BC loadings at Gulou were low in September and October,
266 usually below $6 \mu\text{g}/\text{m}^3$, while the loadings were high in the other months, such as in
267 mid-November, early and late December, early January, and mid-to-late February,
268 suggesting occurrences of BC pollution events during these periods. PM_{2.5} loadings
269 and PM₁₀ loadings were generally below 120 and 200 $\mu\text{g}/\text{m}^3$, respectively, but higher
270 during early October and in the periods when BC loadings were high. The particle
271 concentrations are affected by various factors and progress. For example, the high
272 loadings of particulate matter in early October was mainly due to the increase in
273 aerosols concentrations with high scatter coefficient (SC), and thus the BC loadings
274 did not show such peak during early October.

275

276 Monthly variations of particles in the cold seasons in 2016 were obvious (Fig.2). High



277 particle concentrations were observed from November to February while the low ones
278 were in September and October. The smallest monthly concentrations of BC, PM_{2.5},
279 and PM₁₀ occurred in October, being 1.8, 39.2, and 59.8 µg/m³, respectively, while
280 the largest monthly concentrations occurred in December, being 3.7, 85.0, and 123.1
281 µg/m³, respectively, which were about twice of those in October. In general, there are
282 two key factors that impact particle concentrations: meteorology and emissions.
283 Heavy precipitation with a strong scavenging effect in October might directly lead to
284 small loadings of particles (Table.2). Anthropogenic particle emissions from fossil
285 fuel over China increased after summer and showed a sharp increase from November
286 to January (Zhang et al., 2009), which may explain the high particle concentrations
287 during those periods. Qian et.al (2014) believed that high particle loadings in Nanjing
288 from late October to early November resulted from the large-scale burning of crop
289 residues. However, PM_{2.5} and PM₁₀ concentrations reached a relative maximal in
290 early October, while the emission in October is relative low compared to the
291 following months (Zhang et al., 2009).

292

293 Substantial diurnal cycles of the particles are also observed (Fig.3). BC levels were
294 high at rush hours (7~9 am and 8~11 pm) but low in afternoon (1~3 pm). Zhuang et al.
295 (2014) mentioned that high BC concentrations in these times of the day might be
296 caused by the vehicle emissions (as mentioned in Section 2, several main roads with
297 apparent traffic pollution surround the station). In addition, temperature was low after
298 midnight, and the atmosphere stratification was stable. Therefore, it was easy for



299 temperature inversion to appear, which was not conducive to the diffusion of
300 pollutants, and the concentrations of particles accumulated and reached a peak at
301 around 8 am. Atmosphere stratification became stable again as the temperature
302 decreased after around 4 pm, which may also explain the peak during 9~11 pm (Qian
303 et al., 2014). As to the low BC in afternoon, which occurred at around 3 pm, it was
304 mainly induced by well-developed boundary layer. Because the atmosphere became
305 less stable with increasing temperature, and strong turbulent exchange and vertical
306 diffusion were favorable to the diffusion of pollutants, BC concentrations decreased to
307 a minimum in the afternoon. Fig. 3 also shows that the peak values of fine particle
308 concentrations often occurred one or two hours later than those of BC concentrations,
309 with high values at around 10 am and low values at around 5 pm. According to
310 Khoder (2002), atmospheric photochemical reactions are extremely active under
311 conditions of strong radiation and high temperature, during which more secondary
312 aerosol particles (like sulfate particles) generated, so the concentrations of fine
313 particles in the atmosphere will increase. When solar radiation was strong, ultra-fine
314 particles generated during photochemical reactions contributed greatly to the
315 concentrations of aerosol particles.

316 Generally, the diurnal cycles of BC had a bimodal distribution with two peaks, while
317 $PM_{2.5}$ and PM_{10} had only one peak. However, both magnitude and temporal variations
318 of particles were changed in winter, and there is another peak at around 2 am (see S1),
319 which was possibly due to the affection of BC pollution episodes at night.

320



321 3.2 Characteristics of gaseous pollutants in Nanjing

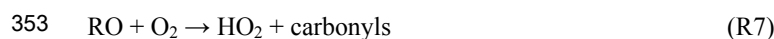
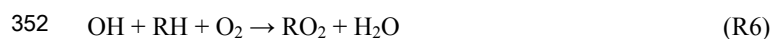
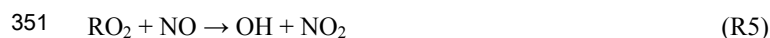
322 Fig.4 shows hourly-mean concentrations of gaseous pollutants at Gulou during the
323 cold seasons in 2016, in which, there were few gaps for invalid values. The averaged
324 concentrations during the fall and winter of CO, O₃, NO_x and NO_y at the site are 851
325 ± 384 , 37.7 ± 33.5 , 23.5 ± 14.7 , and 32.8 ± 22.3 ppb, respectively. As shown in Fig.4,
326 O₃ concentrations in the site were extremely high during the entire September in 2016,
327 with a maximum over 200 ppb, which was mainly due to the strong solar radiation
328 and the high temperature lasting in September. O₃ concentrations began to increase in
329 February because of enhanced solar radiation, after a low-concentration period since
330 late October, during which O₃ concentrations were below 100 ppb. NO_x and NO_y
331 have a similar pattern: the concentrations were high in November, December and
332 February (Fig.5). It is noticeable that the daily variation of CO concentrations was
333 similar to that of BC. A remarkable correlation between BC and CO is found in a
334 number of studies (Jennings et al., 1996; Derwent et al., 2001; Badarinath et al., 2007;
335 Spackman et al., 2008), suggesting that both of the pollutants are greatly affected by
336 anthropogenic sources and biomass burning in eastern China.

337

338 Fig.5 illustrates monthly variations of O₃, nitrogen oxides (NO_y and NO_x), and CO in
339 the cold seasons in 2016. O₃ peaked in September at 74.8 ppb while NO_y and NO_x
340 peaked in December at 31.8 and 41.7 ppb, respectively. O₃ reached minimum at 23.4
341 ppb in November and NO_y and NO_x were lowest in September, being 14.5, and 20.8



342 ppb, respectively. O₃ is a secondary pollutant and complicatedly related to its
343 precursors, including NO_x and VOCs. O₃ precursors and their effects on O₃ formation
344 are different at different geographical locations, and thus the characterizations of O₃ at
345 different sites can vary greatly. O₃-NO_x-VOCs relationships can be described by the
346 following reactions:



354 where (R4), (R5), and (R2) reactions establish an “NO_x cycle” that could produce O₃
355 without consumption of NO_x, the other important chemistry cycle is the so-called
356 “RO_x (RO_x=OH+HO₂ + RO₂) radical cycle” that could continuously supply HO₂ and
357 RO₂ to oxidize NO to NO₂, and (R7) is usually referred as NO_x titration, which is an
358 important O₃ removal process related to freshly emitted NO. In general, when NO_x
359 concentrations were high, O₃ concentrations may experience a depression process
360 since excessive NO are not favorable for the O₃ production (Xie et al, 2016; Wang et
361 al., 2018). The CO concentrations varied greatly in winter because of the frequent
362 shifting of air masses from the clean interior continent and heavily polluted urban
363 plumes in the heating period (normally from November to March in Northern China,



364 (Pan et al., 2011). In September and October, the CO concentrations at Gulou
365 apparently decreased owing to frequent intrusions of clean air mass from the Pacific
366 Ocean, and this seasonal trend was confirmed by HYSPLIT-4 model (see detailed
367 discussion in Section.4).

368

369 Fig. 6 (a) shows the mean diurnal variations of the gaseous pollutants (O_3 , NO_x , NO_y ,
370 and CO) at Gulou during the cold seasons in 2016. The concentrations of O_3 were the
371 lowest around 7 am and went up rapidly corresponding with the increase of solar
372 radiation. After reaching the peak in the middle of the day at 3 pm, the O_3
373 concentrations kept decreasing rapidly until sunset. During the nighttime, the
374 concentrations of O_3 decreased slowly and maintained low values, attributed to the
375 process of NO_x titration and the lack of solar radiation. With respect to NO_x and NO_y ,
376 two peaks appeared in the diurnal cycles, one around 9 am and the other at 8 pm. Both
377 peaks coincided with the rush hours in the city, during which large amounts of vehicle
378 emissions were released. The morning peak was slightly higher than the evening one.
379 The abovementioned diurnal cycles in O_3 and nitrogen oxides concentrations followed
380 the typical patterns in polluted areas (Lal et al., 2000; Lam et al., 2001; Wang et al.,
381 2006; Tu et al., 2007; Ding et al., 2013; Xie et al., 2016). Since CO concentrations
382 showed a diurnal variation similar to that of BC, the two peaks around 9 am and 8~10
383 pm could also result from vehicle emissions at rush hours.

384

385 According to Xie et al. (2016), these diurnal variation patterns of O_3 and NO_x are



386 mainly resulted from the photochemical processes and the meteorological conditions.
387 The ultraviolet irradiance (UV) at Gulou started to increase at about 7 am (Fig.6 (b)),
388 which could induce a series of photochemical reactions including the formation of
389 peroxy radicals (HO_2 and RO_2 etc.) and the photolysis of NO_2 . From 8 am to 3 pm,
390 the increase in UV enhanced the O_3 formation by the production processes of (R4)–
391 (R5). Simultaneous measurement of O_3 and UV shows that the O_3 concentrations are
392 highly correlated to UV, with a correlation coefficient of 0.47. It is also noticeable
393 that the O_3 maximum was 2 h after the UV maximum, suggesting the time to take for
394 the chemical reactions. The slightly reduction of O_3 and NO_x after the midnight is
395 likely due to of NO_x titration. The development of the planetary boundary layer (PBL)
396 can also modulate pollutant concentrations. The concentrations of a pollutant are
397 diluted when PBL rise during the daytime and enhanced in the low nocturnal PBL that
398 favors pollutant accumulation, after comparing Fig.6 (a) with the reported diurnal
399 variation of PBL height in Nanjing (Jiang et al., 2014; Xie et al., 2016).

400

401 Table 7 further provides the statistics of O_3 , $\text{PM}_{2.5}$ and PM_{10} mass concentrations with
402 a comparison to the National Ambient Air Quality Standards in China (NAAQS-CN),
403 which were released in 2012 by the China State Council and will be implemented
404 nationwide in 2016 (MEP, 2012). According to NAAQS-CN for $\text{PM}_{2.5}$ and PM_{10} (75
405 $\mu\text{g}/\text{m}^3$ of $\text{PM}_{2.5}$ concentrations and $150 \mu\text{g}/\text{m}^3$ of PM_{10} concentrations for 24h average),
406 there were 48 days of $\text{PM}_{2.5}$ exceedances, accounting for about 30% of the 6 months
407 period, and 14 days of PM_{10} exceedances, lower than the $\text{PM}_{2.5}$ exceedances. Days of



408 particulate matter exceedances mainly occurred during DJF. Donkelaar et al. (2010)
409 reported that a multi-year average of PM_{2.5} mass concentrations was over 80 µg/m³ in
410 eastern China by using satellite data during 2001–2006, and Ding et al. (2013) stated
411 an 1-year average about 75 µg/m³ in rural area of Nanjing from August 2011 to July
412 2012. Therefore, the means in Table 7 show lower particle concentrations than what
413 were reported. The days of exceedances also were fewer than in 2011 (Ding et al.,
414 2013), during which 99 days of PM_{2.5} exceedances happened during the cold seasons.
415 These results suggest that particles control policies are well-implemented in Nanjing
416 although particles remain a severe pollution problem in the YRD region. According to
417 NAAQS-CN for O₃ (160 µg/m³ for 8 h average and 200 µg/m³ for 1 h average), 37
418 days of exceedances occurred (Table7), covering 20% of the period and mostly
419 appearing in September and February when the air temperature was relatively high. In
420 contrast to particulate matter, O₃ concentrations increased from 2011 to 2016, and the
421 exceedance days were 10 times of those in 2011. It was found in previous studies that
422 O₃ levels in the rural areas were generally higher than those in the city centers (Zhang
423 et al., 2008; Geng et al., 2008; Xie et al., 2016). Thus, high O₃ concentrations and
424 severe air pollution in Gulou, an urban site, suggest a severer O₃ pollution problem in
425 the entire YRD region. Note that this study only discussed the O₃ concentrations in
426 the cold seasons when the concentrations of O₃ are lower than in the warm season,
427 suggest the problem can be severer in the warm seasons. The emissions of O₃
428 precursors (VOCs and NO_y) in Nanjing have significantly increased with the
429 increases of residents (over 200,000 increase since 2011), the number of automobiles



430 (over 65% increase since 2011), and GDP (gross domestic production) (nearly 70%
431 increase since 2011). Consequently, O₃ concentrations at ground level has gradually
432 risen (<http://www.nitj.gov.cn/>).

433

434 3.3 Inter-species correlations

435 Correlations between different species were analyzed to help interpret the data and
436 gain insights into the underlying mechanisms/processes. Because precipitation could
437 impact wet scavenging processes for particles and other aerosols (see S2), we
438 eliminated the data in rainy condition.

439

440 The scatter plot of O₃ measured at the site and NO_x color-coded with air temperature
441 is given in Fig.7 (a). The negative correlation suggests a titration effect of freshly
442 emitted NO with O₃ in the cold seasons. In addition, the slope decreased when air
443 temperature rose. These results suggest a strong photochemical production of O₃ in
444 this region during high air temperature, resulting in the seasonal cycle pattern of O₃
445 shown in Fig. 5 (a) (Ding et.al, 2013). Previous research has shown that visibility has
446 a good correlation with the concentrations of particles and relative humidity. With an
447 increase in the PM_{2.5} concentrations, visibility decreases exponentially (Fig.7 (b)),
448 because the concentrations of particles would increase scattered and absorption
449 extinction coefficients, while the visibility (Vis) is related to the coefficients through:

$$450 \quad Vis = \frac{3.91}{\sigma} \quad (13)$$



451 where V_{is} is the visibility and σ is the extinction coefficient (EC) (Larson et.al,
452 1989). As for the effect of relative humidity (RH) on the visibility, according to Mie
453 theory, with the increase of the relative humidity, the radius of the wet particle
454 increase, and so the extinction coefficient increases. Therefore, the visibility decrease.
455 Moreover, when $RH \leq 80\%$, the effect of particle concentrations on visibility could
456 become smog, and when $80\% < RH \leq 90\%$, the effect could form smog and fog at the
457 same time. Thus, we performed a linear fit of the visibility with differing
458 concentrations of $PM_{2.5}$ when $RH \leq 70\%$, $70\% < RH \leq 80\%$, and $80\% < RH \leq 90\%$, to
459 find out the relationship among these factors. Although there is no precipitation, there
460 are still water droplets in the air when $RH > 90\%$, which become fog. Therefore, we
461 eliminated those data. It is found that the fitting curves are as follows: $[PM_{2.5}] =$
462 $366.72[Vis]^{-0.745}$ ($R^2 = 0.7196$), $[PM_{2.5}] = 337.16[Vis]^{-0.855}$ ($R^2 = 0.8692$), and $[PM_{2.5}]$
463 $= 248.6[Vis]^{-0.852}$ ($R^2 = 0.8279$).

464

465 To figure out the interaction between particles and O_3 , we give scatter plots of $PM_{2.5}$ –
466 O_3 and BC – O_3 (Fig.8), in which data points are color-coded with air temperature.
467 Overall, particulate matters and black carbon are negatively correlated with O_3 ,
468 because particulates inhibit the photolysis reactions near the surface, reducing the
469 photolysis frequencies in the atmosphere, and resulting in the decrease of O_3
470 concentrations near the ground, which is also addressed using the chemical transport
471 model (HANK) (Li et al., 2005). It is noticeable that a negative correlation could be
472 found for low air temperature samples while a pronounced positive correlation existed



473 for high temperature data points. The negative correlation for cold air is mainly due to
474 the titration effect of high NO concentrations, which was associated with high
475 primary PM_{2.5} in the cold seasons as well. And the positive correlation for high air
476 temperature is related to the formation of secondary fine particles associated with high
477 concentrations of O₃, which may be related to high conversion rate of SO₂ to sulfate
478 under high concentrations of oxidants (Khoder, 2002). Previous studies of PM_{2.5}
479 chemical compositions in Shanghai and Nanjing (Wang et al., 2002, 2006) suggested
480 that sulfate was the most dominate ion in PM_{2.5}. The detailed mechanisms still need to
481 be further addressed by long-term measurement of aerosol chemical composition.
482 Since black carbon is insoluble in polar and non-polar solvents and remains stable
483 when air or oxygen is heated to 350 ~ 400°C, it cannot be generated nor cleared
484 through chemical reactions. Thus, when air temperature rises, the correlation between
485 BC and O₃ becomes obscurer compared to the one between PM_{2.5} and O₃. Scatter
486 plots of CO–NO_x, PM_{2.5}–NO_x, and BC–NO_x, are given in Figs. 9(a)-9(c), with data
487 points color-coded with concentrations of O₃. Fig.9 (b) and 9(c) show a good positive
488 correlation between PM_{2.5} and NO_x, as well as BC and NO_x, suggesting that the
489 particles at the site in Nanjing University Gulou Campus were mainly associated with
490 combustion sources, which is also the reason for the negative correlation between
491 particles and O₃. It is found that high O₃ levels are generally associated with air
492 masses of high CO/NO_x or particles/NO_x ratio, and when NO_x concentrations was
493 lower than 40 ppb, an increase in CO or particular matter concentrations would cause
494 a sharp increase in O₃ concentrations while NO_x reverses. As discussed in Atkinson



495 et.al (2000), volatile organic compounds (VOCs) generally have good correlation with
496 CO and play a role similar to CO in the photochemical ozone production. Particles
497 also have good correlation with CO, so the particles–O₃–NO_x relationship may
498 indicate a VOC-sensitive regime of O₃ formation in this region, as the CO–O₃–NO_x
499 relationship. Geng et al. (2008) reported a VOC-sensitive regime in Shanghai by
500 using measured and modeling results, and Ding et al. (2013) also reported a
501 VOC-sensitive regime in rural area in Nanjing.

502

503 Correlations of PM_{2.5}–O₃ in daytime when UV radiation is relatively strong and
504 nighttime when UV radiation is approximately 0 are shown in Fig.10. It is found that
505 the correlation is better with a clearer tendency and O₃ are higher during daytime,
506 suggesting strong photochemistry progresses during daytime. Some data in the
507 nighttime plots show relatively high O₃. Most occurred in September and February
508 when O₃ concentrations were extremely high. It is also found that some show
509 relatively high NO_x associated with relatively low PM_{2.5}. After a further backward
510 trajectories analysis (Section 3.4), we found that these data are most likely
511 corresponded to air masses coming from the nearby and northwest in November and
512 December, which may contain high NO_x plumes and transport to Nanjing during
513 nighttime.

514 **3.4 Backward Trajectories Analysis**

515 The cluster means of the backward trajectories at 100 m from Gulou, Nanjing, in 2016



516 fall (Fig.11) and winter (Fig. 13) suggest different air flows that were transported to
517 Nanjing from long distances. Most of air masses came from the oceans in fall (40 %,
518 cluster 4 in Fig. 11) and from the north and north-west of China in winter (49 %,
519 clusters 1 and 4 in Fig. 13). Although air masses came from north in both fall (cluster
520 4) and winter (cluster 4), the trajectory cluster in fall came from the oceans more than
521 the one in winter. In winter, considerable air masses arriving at the site were also from
522 places near Nanjing (35%, cluster 2 in Fig. 13). Therefore, the aerosol kinds and
523 optical properties at the study site are characterized differently with different air
524 masses in the two seasons, which are further analyzed by their origins in SON and
525 DJF (Figs.12 and 14).

526

527 Figs. 12 and 14 show the main concentrations of particles and trace gases, the ratio of
528 $PM_{2.5}$ to PM_{10} , as well as the values of the aerosol optical properties of different
529 clusters during SON and DJF, respectively. Because PM_{10} vary similarly to $PM_{2.5}$,
530 while NO_x varies similarly to NO_y , we only show the variations of $PM_{2.5}$ and NO_y
531 with cluster here. Also, because AAC, SC and Bsp have good correlations with
532 particle concentrations (Zhuang et al., 2014) and Asp is greatly affected by relative
533 humidity (RH), we discuss the variation of SAE and SSA with cluster here.

534

535 In SON, the dominant air masses are from the East China Sea (passing through urban
536 agglomeration regions (cluster 3), and less-developed regions (cluster 2) of the YRD,
537 and northern continent away from Nanjing (cluster 4) (passing through oceans and



538 urban agglomeration regions). It is found that although air masses in cluster 3, cluster
539 4 and cluster 2 all pass through the oceans and have the same level of relative
540 humidity (RH), differences still exist among the clusters. The air masses have to cross
541 the urban agglomeration (from Shanghai to Nanjing) of YRD when they arrive in
542 Nanjing in cluster 3 but past less-developed regions (north Jiangsu Province) in
543 cluster 4 and cluster 2. In YRD, emissions of the aerosols and trace gases are much
544 stronger in urban agglomeration regions than those in other areas (Zhang et al., 2009;
545 Zhuang et al., 2013). It is also noticeable that concentrations of aerosols in cluster 4
546 are mostly lower, which may result from its avoidance from BTH regions, also a
547 megacities and urban agglomeration. In addition, air masses from the west of cluster 1
548 contain the highest concentrations of particulate matter, CO and NO_y, which may
549 result from crossing central China with high emission of CO according to MERRA
550 data (<https://gmao.gsfc.nasa.gov/reanalysis/MERRA>). Particulate matter and NO_y
551 mainly have the same sources as CO, and high concentrations of these aerosols are
552 also reflected in a high AOD according to the MISR data
553 (<https://giovanni.gsfc.nasa.gov/giovanni>). Zhuang et al. (2015) also suggested that
554 high emission occurred in central China. As for the ratio of PM_{2.5} to PM₁₀, the ratio
555 represents the amount of particles deriving from secondary pollution progress
556 compared to those from primary pollution progress. Clusters 1-3 had relatively similar
557 ratios in SON, all over 60% except cluster 4, with the maximum of cluster 3, which
558 means particles deriving from secondary pollution progress in the three clusters have
559 a similar rate. O₃ concentrations among the four cluster were different. Despite



560 negative correlations of O_3 with its precursors and particles, the concentrations of O_3
561 in cluster 3 was higher than in cluster 4, as UV in cluster 3 was higher than in cluster 4.
562 The size of the aerosols in cluster 1 were finest (SAE is the largest in Fig. 12g),
563 because the other three clusters all passed through oceans before arriving Nanjing,
564 with higher relative humidity (RH), making it easier for particles' hygroscopic growth.
565 SSA is also the largest in cluster 1, which means aerosols in cluster 1 are more
566 scattering.

567

568 In DJF, the air masses were from the places near Nanjing (cluster 2), northern
569 continent away from Nanjing (cluster 1), and northern continent away from Nanjing
570 passing through oceans and urban agglomeration regions (cluster 4). This is different
571 from that in SON. Therefore, besides what has been discussed of cluster 3 and cluster
572 4 in SON, it is found that air masses from cluster 1 and cluster 2 both account for over
573 30% of the total characteristics of the aerosol optical properties and are main sources
574 of pollutants in DJF (particles, CO , and NO_x are higher in Fig.14). Air masses in
575 cluster 1 came from Shandong Province while those in cluster 2 came from areas
576 nearby. Particles and trace gases concentrations of cluster 2 are higher than those of
577 cluster 1 to some extent, which may result from the severer pollution in southern
578 YRD than in Shandong Province. The concentrations of O_3 , similar to that in SON,
579 was affected by the UV (O_3 concentrations in cluster 2 is a little higher than that in
580 cluster 1 in Fig.14). The ratio of $PM_{2.5}$ to PM_{10} of cluster 1 and cluster 2 are
581 approximately equal in DJF, over 70%. The size of aerosols in cluster 1 and 2 are



582 finer without passing through oceans, so SAE are larger (Fig.12g). Aerosols in cluster
583 1 are scatter to some extent compared to those in cluster 2.

584

585 **3.5 Case Study**

586 For further understanding of the causes for high pollutants episodes, especially high
587 particulate and O₃ episodes, we choose a typical episode from 2016 December 3-6 for
588 a detailed analysis.

589

590 Fig.15 (a) and (b) show that high O₃ concentrations (over 80 ppb) occurred on
591 December 4 with broad O₃ peaks (over 60 ppb) in the following days, while the
592 average O₃ during the cold seasons was 37.7 ppb. Though there is a lack of particulate
593 matter concentrations because of the instrument breakdown, we could see the high
594 concentrations of particulate matter from the relatively high EC value (over 500 Mm⁻¹)
595 and BC concentrations (over 6 μg/m³) on December 4th, and both reach a maximum
596 on December 5th (PM_{2.5} over 200 μg/m³ and PM₁₀ over 300 μg/m³), over 3 times of
597 the average concentrations. Besides, NO_x, NO_y, have reached high levels since
598 December 4th (NO_x over 70 ppb and NO_y over 100 ppb). It is also noticeable that
599 SSA has a relatively sharp decrease from December 4, especially on December 5
600 when particle concentrations were extremely high, representing that the ratio of PM₁₀
601 became higher. Meanwhile, a relatively sharp increase occurred in SAE, without any
602 obvious variation in AAE, though, which shows that scattering aerosols are the main



603 components. It is also found that this case occurred under calm conditions before the
604 passage of a cold front, which was at the front of a continental high pressure system
605 originating from Mongolia and sweeping over Nanjing (Fig.15 (c)), and the decrease
606 in temperature with high pressure system dominating eastern China were also
607 detected on December 6. Backward trajectories analysis for the past 96 hours (Fig.15
608 (d)) were conducted for December 5 at 8 pm for the maximum concentrations of O₃
609 on December 4 and particulate matter on December 5, which suggest that
610 predominant wind was just in time from the NW directions. Therefore, air masses
611 with high particles and O₃ concentrations would be transported to Nanjing, which
612 were also clearly detected in Nanjing during these days, such as the relatively high O₃
613 during nighttime on December 5 and 6. The highest O₃ on December 4 together with
614 high particles and primary pollutants NO_x and NO_y suggests a strong in situ
615 photochemical production in mixed regional plumes under the influence of high
616 pressure system. Guo et al. (2009) reported that the anticyclonic conditions, e.g.,
617 sunny weather and low wind velocities, are favorable for pollution accumulation and
618 O₃ production. Results in this case clearly demonstrate sub-regional transport of
619 primary and secondary air pollutants within the YRD region under such weather
620 system.

621 4. Conclusion

622 In this paper, an overview of particles and O₃ concentrations, together with trace gases,
623 during 2016 the cold seasons in urban Nanjing, China, has been presented based on



624 continuous measurements of aerosols concentrations and optical properties at the
625 Gulou site. The particles, O₃ and trace gases concentrations are comprehensively
626 characterized from perspectives of temporal variations, inter-species correlations,
627 trajectories analysis, and case studies based on weather data and Lagrangian
628 dispersion modeling.

629

630 Measurements show that hourly mean particle concentrations, including BC, PM_{2.5},
631 and PM₁₀ at Gulou site, Nanjing, China, are $2.602 \pm 1.720 \mu\text{g}/\text{m}^3$, $58.2 \pm 36.8 \mu\text{g}/\text{m}^3$,
632 and $86.3 \pm 50.8 \mu\text{g}/\text{m}^3$, respectively, with ranges of 0.064-15.608 $\mu\text{g}/\text{m}^3$, 0.8-256.2
633 $\mu\text{g}/\text{m}^3$, and 1.1-343.4 $\mu\text{g}/\text{m}^3$, respectively. During the six months, 48 and 14 days
634 when PM_{2.5} and PM₁₀, respectively, exceeded Class II NAAQS. Measurements also
635 showed that hourly mean O₃ concentrations in urban Nanjing ranged from 0.2 to
636 235.7 ppb, with average concentrations of 37.7 ± 33.5 ppb. There were 40 days excess
637 of O₃ during the period, suggesting a severe air pollution problem in the region.

638

639 The correlation analysis shows a negative PM_{2.5}-Vis correlation as well as RH, both
640 of which would promote the extinction coefficient. Negative O₃-NO_y correlation
641 occurs when temperature is relatively low but the correlation becomes weaker when
642 temperature becomes higher. PM_{2.5}-O₃-T correlations reveal the formation of
643 secondary aerosols, especially fine particulate matter under high O₃ concentration and
644 temperature conditions, while BC-O₃-T correlations not. CO-NO_y-O₃ and PM_{2.5}-
645 NO_y-O₃ correlations suggest that a VOC-sensitive regime for photochemical



646 production of O₃ in urban Nanjing.

647

648 The backward trajectory analysis suggests that the prevailing winds in Nanjing were
649 from the north and east during the cold seasons in 2016. Air masses that are either
650 from the east without passing through the urban agglomeration and from northern
651 without crossing BTH regions were clean with low pollution concentrations. In
652 contrast, air masses from local regions were polluted in winter, suggesting a severe air
653 quality problem in YRD region. SAE and SSA were further studied, indicating that
654 particles from oceans were coarser and less scattering because the airmasses were
655 under high RH condition and less secondary pollutants were produced.

656

657 A case study for a typical high O₃ and PM_{2.5} episode in December 2016 illustrates the
658 important influences of sub-regional transport of pollutants from strong source
659 regions and local synoptic weather on the episode. Stable conditions such as an
660 anticyclonic system make it easy for pollutants to accumulate in this region. Results
661 from this case reveal the mechanisms of sub-regional transport of primary and
662 secondary air pollutants within the YRD region.

663

664 Data availability. The automobile numbers and GDP are from <http://www.njtj.gov.cn/>.
665 Satellite CO data are available at: <https://gmao.gsfc.nasa.gov/reanalysis/MERRA>. The
666 aerosols AOD data are available at: <https://giovanni.gsfc.nasa.gov/giovanni>. The
667 Lagrangian dispersion model Hybrid Single-Particle Lagrangian Integrated Trajectory



668 (HYSPLIT) was supplied by NOAA: http://ready.arl.noaa.gov/HYSPLIT_traj.php.

669 The meteorological data for HYSPLIT are accessible from

670 <ftp://arlftp.arlhq.noaa.gov/pub/archives/gdas1>.

671

672 **Acknowledgements:** This work was supported by the National Key R&D Program of China

673 (2017YFC0209803, 2014CB441203, 2016YFC0203303), the National Natural Science

674 Foundation of China (41675143, 91544230, 41621005). The authors would like to thank all

675 members in the AERC of Nanjing University for maintaining instruments.

676

677 **Reference:**

678 Allen, R. J., Sherwood, S. C., Norris, J. R., and Zender, C.S.: Recent Northern Hemisphere tropical

679 expansion primarily driven by black carbon and tropospheric ozone, *Nature*, 485,

680 doi:10.1038/nature11097, 350–353, 2012.

681 Anderson, T. L. and Ogren, J. A.: Determining aerosol radiative properties using the TSI 3563

682 integrating nephelometer, *Aerosol Sci. Tech.*, 29, 57–69, 1998.

683 Andrews, E., Sheridan, P. J., Fiebig, M., McComiskey, M., Ogren, J. A., Arnott, P., Covert, D.,

684 Elleman, R., Gasparini, R., Collins, D., Jonsson, H., Schmid, B., and Wang, J.: Comparison of

685 methods for deriving aerosol asymmetry parameter, *J. Geophys. Res.*, 111, D05S04,

686 doi:10.1029/2004JD005734, 2006.

687 Arnott, W. P., Hamasha, K., Moosmuller, H., Sheridan, P. J., and Ogren, J. A.: Towards aerosol

688 light-absorption measurements with a 7-wavelength aethalometer: evaluation with a

689 photoacoustic instrument and 3-wavelength nephelometer, *Aerosol Sci. Technol.*, 39, 17–29,



- 690 doi:10.1080/027868290901972, 2005.
- 691 Atkinson, R.: Atmospheric chemistry of VOCs and NO_x, *Atmos. Environ.*, 34, 2063–2101,
- 692 doi:10.1016/S1352-2310(99)00460-4, 2000.
- 693 Badarinath, K. V. S., Kharol, S. K., Chand, T. R. K., Parvathi, Y. G., Anasuya, T., and Jyothisna, A. N.:
- 694 Variations in black carbon aerosol, carbon monoxide and ozone over an urban area of Hyderabad,
- 695 India, during the forest fire season, *Atmos. Res.*, 85(1), 18–26, 2007.
- 696 Bond, T. C., Doherty, S. J., Fahey, D. W., Forster, P. M., Berntsen, T., DeAngelo, B. J., Flanner, M. G.,
- 697 Ghan, S., Karcher, B., Koch, D., Kinne, S., Kondo, Y., Quinn, P. K., Sarofim, M. C., Schultz, M.
- 698 G., Schulz, M., Venkataraman, C., Zhang, H., Zhang, S., Bellouin, N., Guttikunda, S. K., Hopke,
- 699 P. K., Jacobson, M. Z., Kaiser, J. W., Klimont, Z., Lohmann, U., Schwarz, J. P., Shindell, D.,
- 700 Storlvmo, T., Warren, S. G., and Zender, C. S.: Bounding the role of black carbon in the climate
- 701 system: A scientific assessment, *J. Geophys. Res.: Atmos.*, 118, 5380–5552,
- 702 doi:10.1002/jgrd.50171, 2013.
- 703 Bond, T. C., Streets, D. G., Yarber, K. F., Nelson, S. M., Woo, J.-H., and Klimont, Z.: A
- 704 technology-based global inventory of black and organic carbon emissions from combustion, *J.*
- 705 *Geophys. Res.*, 109(D14), D14203, doi:10.1029/2003jd003697, 2004.
- 706 Castro, T., Madronich, S., Rivale, S., Muhlia, A., and Mar, B.: The influence of aerosols on
- 707 photochemical smog in Mexico City, *Atmos. Environ.*, 35, 1765–1772, 2001.
- 708 Chameides, W.L., Bergin, M., 2002. Soot takes center stage. *Science* 297 (5590), 2214–2215.
- 709 Chan, C.K., Yao, X., 2008. Air pollution in mega cities in China. *Atmos. Environ.* 42, 1–42.
- 710 Collaud Coen, M., Weingartner, E., Apituley, A., Ceburnis, D., Fierz-Schmidhauser, R., Flentje, H.,
- 711 Henzing, J. S., Jennings, S. G., Moerman, M., Petzold, A., Schmid, O., and Baltensperger, U.:



- 712 Minimizing light absorption measurement artifacts of the Aethalometer: evaluation of five
713 correction algorithms, *Atmos. Meas. Tech.*, 3, 457–474, doi:10.5194/amt-3-457-2010, 2010.
- 714 Crutzen P. 1973. A discussion of the chemistry of some minor constituents in the stratosphere and
715 troposphere[J]. *Pure Appl. Geophys.*, 106-108 (1): 1385-1399, doi: 10.1007/BF00881092.
- 716 Deng, J.J., Wang, T.J., Liu, L., Jiang, F.: Modeling heterogeneous chemical processes on aerosol
717 surface. *Particuology* 8 (4), 308-318, 2010.
- 718 Derwent, R. G., Ryall, D. B., Jennings, S. G., Spain, T. G., and Simmonds, P. G.: Black carbon aerosol
719 and carbon monoxide in European regionally polluted air masses at Mace Head, Ireland during
720 1995–1998, *Atmos. Environ.*, 35(36), 6371–6378, 2001.
- 721 Ding, A. J., Fu, C. B., Yang, X. Q., Sun, J. N., Zheng, L. F., Xie, Y. N., Herrmann, E., Nie, W., Petaja,
722 T., Kerminen, V. -M., and Kulmala, M.: Ozone and fine particle in the western Yangtze River
723 Delta: an overview of 1 yr data at the SORPEs station, *Atmos. Chem. Phys.*, 13, 5813–5830,
724 2013b.
- 725 Draxler, R. R. and Hess, G. D.: An overview of the HYSPLIT 4 modeling system for trajectories
726 dispersion and deposition, *Aust. Meteor. Mag.*, 47, 295–308, 1998.
- 727 Draxler, R.R. and Rolph, G.D. (2013) HYSPLIT (HYbrid Single-Particle Lagrangian Integrated
728 Trajectory) Model Access Via NOAA ARL READY Website, NOAA Air Resources Laboratory,
729 Silver Spring, MD [online].
- 730 Gao, J., Wang, T., Ding, A., and Liu, C.: Observational study of ozone and carbon monoxide at the
731 summit of mount Tai (1534 m a.s.l.) in central-eastern China. *Atmos. Environ.* 39, 4779–4791,
732 2005.
- 733 Geng, F.H., Tie, X.X., Xu, J.M., Zhou, G.Q., Peng, L., Gao, W., Tang, X., Zhao, C.S.:



- 734 Characterizations of ozone, NO_x, and VOCs measured in Shanghai, China. *Atmos. Environ.* 42,
735 6873–6883, 2008.
- 736 Jacobson, M.Z., 2002. Control of fossil-fuel particulate black carbon and organic matter, possibly the
737 most effective method of slowing global warming. *Journal of Geophysical Research* 107 (D19),
738 4410.
- 739 Jacobson, M. Z.: Studying the effects of aerosols on vertical photolysis rate coefficient and temperature
740 profiles over an urban airshed, *J. Geophys. Res.*, 103, 10593–10604, doi:10.1029/95J00287,
741 1998.
- 742 Jennings, S. G., Spain, T. G., Doddridge, B. G., Maring, H., Kelly, B. P., and Hansen, A. D. A.:
743 Concurrent measurements of black carbon aerosol and carbon monoxide at Mace Head, *J.*
744 *Geophys. Res.-Atmos.*, 101(D14), 19447–19454, 1996.
- 745 Jiang, J., Zheng, Y.F., Liu, J.J., and Fan, J.J.: Observational research on planetary boundary layer by
746 lidar over Nanjing city. *Environ. Sci. Technol.* 37, 22–27 (in Chinese), 2014.
- 747 Kaufman, Y.J.; Tanré, D.; Boucher, O. A satellite view of aerosols in the climate system. *Nature* 2002,
748 419, 215–223.
- 749 Kristjánsson, J.E., 2002. Studies of the aerosol indirect effect from sulfate and black carbon aerosols.
750 *Journal of Geophysical Research* 107 (D15), 4246.
- 751 Khoder, M. I.: Atmospheric conversion of sulfur dioxide to particulate sulfate and nitrogen dioxide to
752 particulate nitrate and gaseous nitric acid in an urban area, *Chemosphere*, 49, 675–684, 2002.
- 753 Lal, S., Naja, M., and Subbaraya, B.H.: Seasonal variations in surface ozone and its precursors over an
754 urban site in India. *Atmos. Environ.* 34, 2713–2724, 2000.
- 755 Lam, K.S., Wang, T.J., Chan, L.Y., Wang, T., and Harris, J.: Flow patterns influencing the seasonal



- 756 behavior of surface ozone and carbon monoxide at a coastal site near Hong Kong. Atmos.
757 Environ. 35, 3121–3135, 2001.
- 758 Larson, S.M., and Cass, G.R.: Characteristics of summer midday low-visibility events in the Los
759 Angeles area. Environmental Science & Technology. 23-281, 1989.
- 760 Liao, H., Seinfeld, J.H., 2005. Global impacts of gas-phase chemistry aerosol interactions on direct
761 radiative forcing by anthropogenic aerosols and ozone. Journal of Geophysical Research 110,
762 D18208.
- 763 Li, G.H., Zhang, R.Y., and Fan, J.W.: Impacts of black carbon aerosol on photolysis and ozone. [J].
764 Journal of Geophysical Research. Vol. 110, D23206, doi:10.1029/2005JD005898, 2005.
- 765 Li, J., Wang, Z., Wang, X., Yamaji, K., Takigawa, M., Kanaya, Y., Pochanart, P., Liu, Y., Irie, H., Hu,
766 B., Tanimoto, H., and Akimoto, H.: Impacts of aerosols on summertime tropospheric photolysis
767 frequencies and photochemistry over Central Eastern China, Atmos. Environ., 45, 1817–1829,
768 doi:10.1016/j.atmosenv.2011.01.016, 2011.
- 769 Lin, W., Xu, X., Ge, B., Zhang, X., 2009. Characteristics of gaseous pollutants at Gucheng, a rural site
770 southwest of Beijing. J. Geophys. Res.-Atmos. 114, D00G14.
- 771 Luo, C., St. John, J. C., Zhou, X. J., Lam, K. S., Wang, T., and Chameides, W. L.: A nonurban ozone
772 air pollution episode over eastern China: Observation and model simulation, J. Geophys. Res.,
773 105, 1889–1908, 2000.
- 774 Ma, J.Z., Xu, X.B., Zhao, C.S., Yan, P., 2012. A review of atmospheric chemistry research in China:
775 photochemical smog, haze pollution, and gas-aerosol interactions. Adv. Atmos. Sci. 29, 1006–
776 1026.
- 777 McGowan, H. and Clark, A.: Identification of dust transport pathways from Lake Eyre, Australia using



- 778 Hysplit, Atmos. Environ., 42, 6915–6925, 2008.
- 779 Müller, T., Laborde, M., Kassell, G., and Wiedensohler, A.: Design and performance of a
780 three-wavelength LED-based total scatter and backscatter integrating nephelometer, Atmos. Meas.
781 Tech., 4, 1291–1303, doi:10.5194/amt-4-1291-2011, 2011.
- 782 Monks, P.S., Archibald, A.T., Colette, A., Cooper, O., Coyle, M., Derwent, R., Fowler, D., Granier, C.,
783 Law, K.S., Mills, G.E., Stevenson, D. S., Tarasova, O., Thouret, V., von Schneidmesser, E.,
784 Sommariva, R., Wild, O., and Williams, M. L.: Tropospheric ozone and its precursors from the
785 urban to the global scale from air quality to short-lived climate forcer, Atmos. Chem. Phys., 15,
786 8889–8973, doi:10.5194/acp-15-8889-2015, 2015.
- 787 Tropospheric ozone and its precursors... (PDF Download Available). Available from:
788 [https://www.researchgate.net/publication/278623484_Tropospheric_ozone_and_its_precursors_fr](https://www.researchgate.net/publication/278623484_Tropospheric_ozone_and_its_precursors_from_the_urban_to_the_global_scale_from_air_quality_to_short-lived_climate_forcer#pdf)
789 om_the_urban_to_the_global_scale_from_air_quality_to_short-lived_climate_forcer#pdf
790 [accessed Jun 24 2018].
- 791 Pan, X.L., Kanaya, Y., Wang, Z.F., Liu, Y., Pochanart, P., Akimoto, H., Sun, Y.L., Dong, H.B., Li, J.,
792 Irie, H., Takigawa, M., 2011. Correlation of black carbon aerosol and carbon monoxide in the
793 high-altitude environment of Mt. Huang in Eastern China. Atmospheric Chemistry and Physics 11,
794 9735-9747.
- 795 Petzold, A., Kopp, C., and Niessner, R.: The dependence of the specific attenuation cross-section on
796 black carbon mass fraction and particle size, Atmos. Environ., 31, 661–672, 1997.
- 797 Qian, L., Yan, Y., and Qian, J.M.: An Observational Study on Physical and Optical Properties of
798 Atmospheric Aerosol in Autumn in Nanjing [J]. Meteorological and Environmental Research
799 2014, 5(2): 24 - 30



- 800 Schmid, O., Artaxo, P., Arnott, W. P., Chand, D., Gatti, L. V., Frank, G. P., Hoffer, A., Schnaiter, M.,
801 and Andreae, M. O.: Spectral light absorption by ambient aerosols influenced by biomass burning
802 in the Amazon Basin. I: Comparison and field calibration of absorption measurement techniques,
803 Atmos. Chem. Phys., 6, 3443–3462, doi:10.5194/acp-6-3443-2006, 2006.
- 804 Schneidemesser, E., Sommariva, R., Wild, O., and Williams, M. L.: Tropospheric ozone and its
805 precursors from the urban to the global scale from air quality to short-lived climate forcer, Atmos.
806 Chem. Phys., 15, 8889–8973, doi:10.5194/acp-15-8889-2015, 2015.
- 807 Song, W.; Jia, H.; Huang, J.; Zhang, Y. A satellite-based geographically weighted regression model for
808 regional PM_{2.5} estimation over the Pearl River Delta region in China. Remote Sens. Environ.
809 2014, 154, 1–7.
- 810 Spackman, J. R., Schwarz, J. P., Gao, R. S., Watts, L. A., Thomson, D. S., Fahey, D. W., Holloway, J.
811 S., de Gouw, J. A., Trainer, M., and Ryerson, T. B.: Empirical correlations between black carbon
812 aerosol and carbon monoxide in the lower and middle troposphere, Geophys. Res. Lett., 35(19),
813 L19816, doi:10.1029/2008GL035237, 2008.
- 814 Stein, A. F., Draxler, R. R., Rolph, G. D., Stunder, B. J. B., Cohen, M. D., and Ngan, F.: NOAA'S
815 Hysplit Atmospheric Transport and Dispersion Modeling System, Bull. Amer. Meteor. Soc., 96,
816 2059–2077. doi: <http://dx.doi.org/10.1175/BAMS-D-14-00110.1>, 2016.
- 817 Tu, J., Xia, Z. G., Wang, H. S., and Li, W. Q.: Temporal variations in surface ozone and its precursors
818 and meteorological effects at an urban site in China, Atmos. Res., 85, 310–337, 2007.
- 819 van Donkelaar, A., Martin, R. V., Brauer, M., Kahn, R., Levy, R., Verduzco, C., and Villeneuve, P. J.:
820 Global estimates of ambient fine particulate matter concentrations from satellite-based aerosol
821 optical depth: development and application, Environ. Health Perspectives, 118, 847–855, 2010.



- 822 Virkkula, A., Makela, T., Hillamo, R., Yli-Tuomi, T., Hirsikko, A., Hameri, K., and Koponen, I. K.: A
823 simple procedure for correcting loading effects of aethalometer data, *J. Air Waste Manage.*, 57,
824 1214–1222, doi:10.3155/1047-3289.57.10.1214, 2007.
- 825 Wang, G. H., Huang, L. M., Gao, S. X., Gao, S. T., and Wang, L.S.: Characterization of watersoluble
826 species of PM10 and PM2.5 aerosols in urban area in Nanjing, China, *Atmos. Environ.*, 36, 1299–
827 1307, 2002.
- 828 Wang, M.Y., Cao, C.X., Li, G.S., and Singh, R.P.: Analysis of a severe prolonged regional haze
829 episode in the Yangtze River Delta, China, *Atmos. Environ.*, 102, 112–121, 2015.
- 830 Wang, T., Xue, L. K., Brimblecombe, P., Lam, Y.F., Li, L., and Zhang, L.: Ozone pollution in China:
831 A review of concentrations, meteorological influences, chemical precursors, and effects. *Science*
832 *of the Total Environment.*, 575, 1582–1596, 2017.
- 833 Wang, T.J., Lam, K.S., Xie, M., Wang, X.M., Carmichael, G., and Li, Y.S.: Integrated studies of a
834 photochemical smog episode in Hong Kong and regional transport in the Pearl River Delta of
835 China. *Tellus Ser. B Chem. Phys. Meteorol.* 58, 31–40, 2006.
- 836 Wang, T. J., Zhuang, B. L., Li, S., Liu, J., Xie, M., Yin, C. Q., Zhang, Y., Yuan, C., Zhu, J. L., Ji, L. Q.,
837 and Han, Y.: The interactions between anthropogenic aerosols and the East Asian summer
838 monsoon using RegCCMS. *J. Geophys. Res. Atmos.*, 120, doi:10.1002/2014JD022877, 2015.
- 839 Wang, X., Li, J., Zhang, Y., Xie, S., Tang, X., 2009b. Ozone source attribution during a severe
840 photochemical smog episode in Beijing, China. *Sci. China, Ser. B: Chem.* 52, 1270–1280.
- 841 Wang, Y.Q., Stein, A.F., Draxler, R.R., de la Rosa, J.D., and Zhang, X.Y.: Global sand and dust
842 storms in 2008: Observation and HYSPLIT model verification, *Atmos. Environ.*, 45, 6368–6381,
843 2011.



- 844 Wang, Y., Zhuang, G. S., Zhang, X. Y., Huang, K., Xu, Chang, Tang, A. H., Chen, J. M., and An, Z. S.:
845 The ion chemistry, seasonal cycle, and sources of PM_{2.5} and TSP aerosol in Shanghai, Atmos.
846 Environ., 40, 2935–2952, 2006.
- 847 Weingartner, E., Saathoff, H., Schnaiter, M., Streit, N., Bitnar, B., and Baltensperger, U.: Absorption of
848 light by soot particles: determination of the absorption coefficient by means of aethalometers, J.
849 Aerosol Sci., 34, 1445–1463, doi:10.1016/S0021-8502(03)00359-8, 2003.
- 850 Wu, D., Wu, C., Liao, B., Chen, H., Wu, M., Li, F., Tan, H., Deng, T., Li, H., Jiang, D., and Yu, J. Z.:
851 Black carbon over the South China Sea and in various continental locations in South China,
852 Atmos. Chem. Phys., 13, 12257–12270, doi:10.5194/acp-13-12257-2013, 2013.
- 853 Wu, Y., Guo, J., Zhang, X., Tian, X., Zhang, J., Wang, Y., Duan, J., Li, X. Synergy of satellite and
854 ground based observations in estimation of particulate matter in eastern China. Sci. Total Environ.
855 2012, 433, 20–30.
- 856 Xiao, Z., Bi, X., Feng, Y., Wang, Y., Zhou, J., Fu, X., Weng, Y., 2012. Source apportionment of
857 ambient PM₁₀ and PM_{2.5} in urban area of Ningbo City. Res. Environ. Sci. (China) 5, 549–555.
- 858 Xie, M., Zhu, K.G., Wang, T.J., Chen, P.L., Han, Y., Li, S., Zhuang, B.L., and Shu, L., Temporal
859 characterization and regional contribution to O₃ and NO_x at an urban and a suburban site in
860 Nanjing, China. Science of the Total Environment., 551–552, 533–545, 2016
- 861 Yang, Y., Liu, X., Qu, Y., Wang, J., An, J., Zhang, Y., Zhang, F.: Formation mechanism of continuous
862 extreme haze episodes in the megacity Beijing, China, in January 2013. Atmos. Res. 155, 192–
863 203, 2015.
- 864 Yan, P., Tang, J., Huang, J., Mao, J. T., Zhou, X. J., Liu, Q., Wang, Z. F., and Zhou, H. G.: The
865 measurement of aerosol optical properties at a rural site in Northern China, Atmos. Chem. Phys.,



- 866 8, 2229–2242, doi:10.5194/acp-8-2229-2008, 2008.
- 867 Yi, R., Wang, Y.L., Zhang, Y.J., Shi, Y., Li, M.S., 2015. Pollution characteristics and influence factors
- 868 of ozone in Yangtze River Delta. *Acta Sci. Circumst.* 35, 2370–2377 (in Chinese).
- 869 Yu, J., Wang, W., Zhou, J., Xu, D., Zhao, Q., He, L., 2015. Analysis of pollution characteristics and
- 870 sources of PM_{2.5} in winter of Ningbo City. *Environ. Sci. Technol. (China)* 8, 150–155.
- 871 Zhang, Q., Streets, D.G., Carmichael, G.R., He, K.B., Huo, H., Kannari, A., Klimont, Z., Park, I.S.,
- 872 Reddy, S., Fu, J.S., Chen, D., Duan, L., Lei, Y., Wang, L.T., Yao, Z.L., 2009. Asian emissions in
- 873 2006 for the NASA INTEX-B mission. *Atmos. Chem. Phys.* 9, 5131–5153.
- 874 Zheng, J., Zhong, L., Wang, T., Louie, P.K.K., Li, Z., 2010. Ground-level ozone in the Pearl River
- 875 Delta region: analysis of data from a recently established regional air quality monitoring network.
- 876 *Atmos. Environ.* 44, 814–823.
- 877 Zhang, Y.H., Hu, M., Zhong, L.J., Wiedensohler, A., Liu, S.C., Andreae, M.O., Wang, W., Fan, S.J.:
- 878 Regional integrated experiments on air quality over Pearl River Delta 2004 (PRIDE-PRD2004):
- 879 overview. *Atmos. Environ.* 42, 6157–6173, 2008.
- 880 Zhu, J.L., Wang, T.J., Talbot, R.H., Mao, H.T., Hall, C.B., Yang, X.Q., Fu, C.B., Zhuang, B.L., Li, S.,
- 881 Han, Y., Huang, X., 2012. Characteristics of atmospheric Total Gaseous Mercury (TGM)
- 882 observed in urban Nanjing, China. *Atmospheric Chemistry and Physics* 12, 12103-12118.
- 883 Zhuang, B.L., Liu, L., Shen, F.H., Wang, T.J., Han, Y., 2010. Semidirect radiative forcing of internal
- 884 mixed black carbon cloud droplet and its regional climatic effect over China. *Journal of*
- 885 *Geophysical Research* 115, D00K19.
- 886 Zhuang, B.L., Liu, Q., Wang, T.J., Yin, C.Q., Li, S., Xie, M., Jiang, F., Mao, H.T., 2013. Investigation
- 887 on semi-direct and indirect climate effects of fossil fuel black carbon aerosol over China.



- 888 Theoretical and Applied Climatology 114, 651-672.
- 889 Zhuang, B. L., Li, S., Wang, T. J., Deng, J. J., Xie, M., Yin, C. Q., and Zhu, J. L.: Direct radiative
- 890 forcing and climate effects of anthropogenic aerosols with different mixing states over China,
- 891 Atmos. Environ., 79, 349–361, doi:10.1016/j.atmosenv.2013.07.004, 2013b.
- 892 Zhuang, B. L., Wang, T. J., Liu, J., Li, S., Xie, M., Han, Y., Chen, P. L., Hu, Q. D., Yang X.Q., Fu, C.
- 893 B., and Zhu, J. L.: The surface aerosol optical properties in the urban area of Nanjing, west GTH
- 894 River Delta, China. Atmos. Chem. Phys., 17, 1143–1160, doi:10.5194/acp-17-1143-2017, 2017.
- 895 Zhuang, B. L., Wang, T. J., Liu, J., Ma, Y., Yin, C. Q., Li, S., Xie, M., Han, Y., Zhu, J. L., Yang, X. Q.,
- 896 and Fu, C. B.: Absorption coefficient of urban aerosol in Nanjing, west Yangtze River Delta,
- 897 China, Atmos. Chem. Phys., 15, 13633–13646, doi:10.5194/acp-15-13633-2015, 2015.

898 **Figure Caption**

- 899 Fig 1. Time series of the concentrations of PM₁₀, PM_{2.5}, and BC from September 2016 to February
- 900 2017 at Gulou site, Nanjing, China.
- 901 Fig 2. Seasonal variations of (a) BC, (b) PM_{2.5}, and (c) PM₁₀. Red markers represent the monthly
- 902 averages at Gulou site, Nanjing, China.
- 903 Fig 3. 6-month mean diurnal variations of BC, PM_{2.5}, and PM₁₀ at Gulou site, Nanjing, China
- 904 from September 2016 to February 2017.
- 905 Fig.4 Time series of particles from September 2016 to February 2017 at Gulou site.
- 906 Fig 5. Seasonal variations of (a) O₃, (b) NO_x, (c) CO, and (d) NO_y. The 10, 25, 50, 75, and 90%
- 907 percentile values of each are shown in black, and red markers represent the monthly averages.
- 908 Fig 6. 6-month mean diurnal variations of (a) trace gases and (b) UV (ultra-violet radiation) at



909 Gulou site from September 2016 to February 2017.

910 Fig 7. Scatter plots of (a) O₃-NO_x color-coded with air temperature (T) and (b) PM_{2.5}-Vis
911 color-coded with relative humidity (RH).

912 Fig 8. Scatter plots of (a) PM_{2.5}-O₃ and (b) BC-O₃ color-coded with air temperature (T).
913 Fig 9. Scatter plots of (a) CO-NO_x, (b) PM_{2.5}-NO_x, and (c) BC-NO_x color-coded with O₃.

914 Fig 10. Scatter plots of PM_{2.5}-NO_x color-coded with O₃ during (a) daytime (9:00~ 17:00) and (b)
915 nighttime (0:00~ 6:00).

916 Fig 11. Clusters of 96 h back trajectories arriving at the study site at 100 m in 2016 fall.
917 Fig 12. The 10, 25, 50, 75, and 90% percentile values in each cluster of back trajectories in 2016
918 fall of (a) BC, (b) PM_{2.5}, (c) PM_{2.5}/PM₁₀, (d) CO, (e) O₃, (f) NO_y, (g) SAE, and (h) SSA. Black
919 markers represent the averages.

920 Fig 13. Clusters of 96 h back trajectories arriving at the study site at 100m in 2016 winter.
921 Fig 14. The 10, 25, 50, 75, and 90% percentile values in each cluster of back trajectories in 2016
922 winter of (a) BC, (b) PM_{2.5}, (c) PM_{2.5}/PM₁₀, (d) CO, (e) O₃, (f) NO_y, (g) SAE, and (h) SSA. Black
923 markers represent the averages.

924 Fig 15. Time series during December 3-6, 2016, for (a) PM_{2.5}, BC and O₃ with associated
925 meteorological parameters, trace gases and (b) optical parameters. Red markers represent O₃ over
926 daily maximum average during winter. Weather charts on (c) 4th and (d) 5th December. (f) 96h
927 backward trajectories analysis ending at 1200 UTC on 5th December

928

929

930

931

932

933 **Table**

934 Table 1 Measurements at Gulou site.

Measurement		Instrument	Resolution
Meteorological parameters	T (°C)	Thermo Instruments, THOM 1405-DF	
	P (atm)	Thermo Instruments, THOM 1405-DF	
	RH (%)	Thermo Instruments, THOM 1405-DF	
	Rainfall (mm)		
	Vis (m)	Visibility Meter, GSN-1	
	UV (W/m ²)		
Particles	BC (ng/m ³)	Aethalometer, Model AE-31	1 ng/m ³
	PM _{2.5} (µg/m ³)	Thermo Instruments, THOM 1405-DF	0.1 µg/m ³
	PM ₁₀ (µg/m ³)	Thermo Instruments, THOM 1405-DF	0.1 µg/m ³
Gaseous pollutant	CO (ppb)	Thermo Instruments, TEI 48i	1 ppb
	NO _x (ppb)	Thermo Instruments, TEI 42i	0.4 ppb
	NO _y (ppb)	Thermo Instruments, TEI 42iY	0.4 ppb
	O ₃ (ppb)	Thermo Instruments, TEI 49i	0.01 ppb
Optical parameters	SC (Mm ⁻¹)	Nephelometer, Aurora 3000	10 ⁻³ Mm ⁻¹
	BSP (Mm ⁻¹)	Nephelometer, Aurora 3000	10 ⁻³ Mm ⁻¹
	AAC (Mm ⁻¹)	Aethalometer, Model AE-31	10 ⁻³ Mm ⁻¹

935

936

937 Table 2 Statistics of general meteorological parameters at Gulou site for the 6-month period

938 September 2016~ February 2017.

Month	Temp (°C)	Pres (hPa)	RH (%)	Rainfall (mm)	Vis (km)	UV (W/m ²)
Sep	24.88	996.97	69.41	2.34	11.84	10.36
Oct	18.37	1003.01	85.01	3.12	9.07	5.28
Nov	12.36	1007.87	77.15	1.19	8.99	5.67
Dec	8.74	1010.53	70.33	0.81	7.61	5.03
Jan	6.49	1010.89	70.65	0.59	9.23	4.94
Feb	7.72	1009.65	59.99	0.45	10.24	7.04

939



940

941 Table3.a Nephelometer correction factors for angular nonidealities. Wavelengths for Aurora 3000

942 are 450 nm (B), 525 nm (G), and 635 nm (R), respectively.

Midpoint±half range of calculated correction factors						
wavelength	total scatter			back scatter		
	B	G	R	B	G	R
	1.37±0.29	1.38±0.31	1.36±0.29	0.963±0.040	0.971±0.047	0.968±0.043

943

944

945 Table3.b Correction factors for total scatter as function of Ångström exponent: $C_{ts} = a + b \cdot \alpha_{ts}^*$.

946 For correction of scattering coefficients for the blue (B) wavelength the Ångström exponent

947 calculated from uncorrected scattering coefficients of blue and green (B/G) is used. At the

948 wavelength G and R Ångström exponents at the wavelength pairs B/R and G/R are used,

949 respectively.

wavelength	B		G		R	
Ångström exponents	$\alpha_{ts}^*(B/G)$		$\alpha_{ts}^*(B/R)$		$\alpha_{ts}^*(G/R)$	
parameters	a	b	a	b	a	b
	1.455	-0.189	1.434	-0.176	1.403	-0.156

950

951

952 Table 4 Statistics of general aerosol optical parameters at Gulou for the 6-month period September

953 2016–February 2017.

Factors	Mean ± STD	Median	Maximum	Minimum
550 nm AAC (Mm^{-1})	23.741 ± 15.557	20.568	127.167	0.994
550 nm SC (Mm^{-1})	349.502 ± 235.291	300.901	1873.620	17.436
550 nm BSp (Mm^{-1})	35.469 ± 21.488	31.637	161.958	1.383
550 nm EC (Mm^{-1})	373.536 ± 247.877	323.070	1947.900	22.198
550 nm SSA	0.929 ± 0.028	0.933	0.985	0.743
550 nm Asp	0.645 ± 0.052	0.648	0.902	0.386



470/660 nm AAE	1.600 ± 0.175	1.611	2.822	0.059
450/635 nm SAE	1.192 ± 0.288	1.192	2.159	0.256

954 Table5. Statistics of the three particles during the study period at Gulou site, Nanjing, China

	Mean ± STD	Median	Maximum	Minimum
BC (µg/m ³)	2.602 ± 1.720	2.241	15.609	0.064
PM _{2.5} (µg/m ³)	58.2 ± 36.8	49.3	256.2	0.8
PM ₁₀ (µg/m ³)	86.3 ± 50.8	76.7	343.4	1.1

955

956

957 Table6. Statistics of trace gases during the study period

	Mean ± STD	Median	Maximum	Minimum
CO (ppb)	851 ± 384	765	2852	176
O ₃ (ppb)	37.7 ± 33.5	31.0	235.7	0.2
NO _x (ppb)	23.5 ± 14.7	19.5	80.0	2.7
NO _y (ppb)	32.8 ± 22.3	26.7	158.4	3.6

958

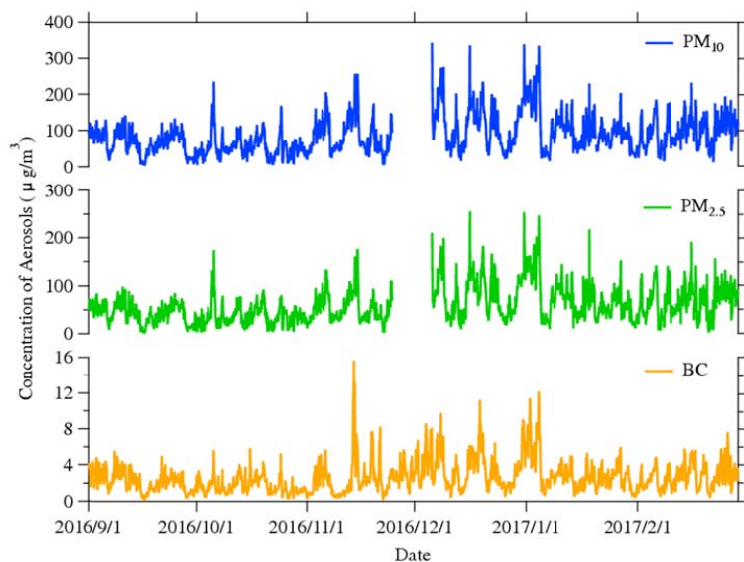
959

960 Table7. Statistics of maximum and number of exceedances of O₃ and PM_{2.5} compared with the

961 National Ambient Air Quality Standards in China.

Aerosol	Mean ± STD (µg/m ³)	Max (µg/m ³)	N.o.E.
PM _{2.5}	58.2 ± 36.8	256.2	48
PM ₁₀	86.3 ± 50.8	343.4	14
O ₃	80.8 ± 71.8	235.7	37

962 N.o.E. of PM_{2.5} accounts for days with 24 h average over 75 µg/m³. N.o.E. of PM₁₀ accounts for days963 with 24 h average over 150 µg/m³. N.o.E of O₃ accounts for days with maximum 8 h average exceed964 160 µg/m³.



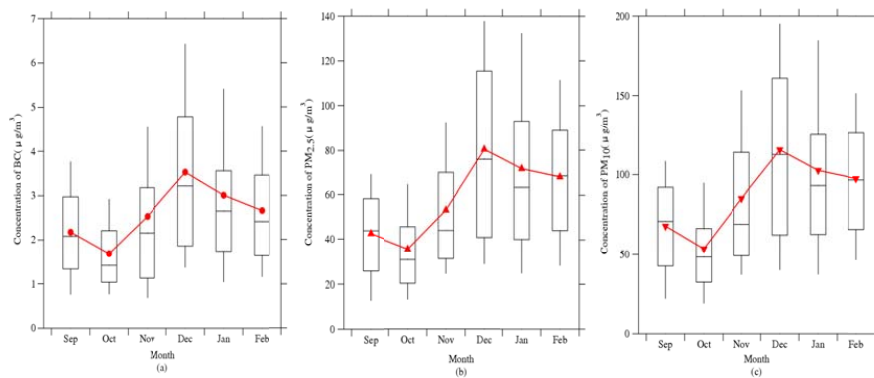
966

968 Fig 1. Time series of the concentrations of PM₁₀, PM_{2.5}, and BC from September 2016 to February

969

2017 at Gulou site, Nanjing, China.

969



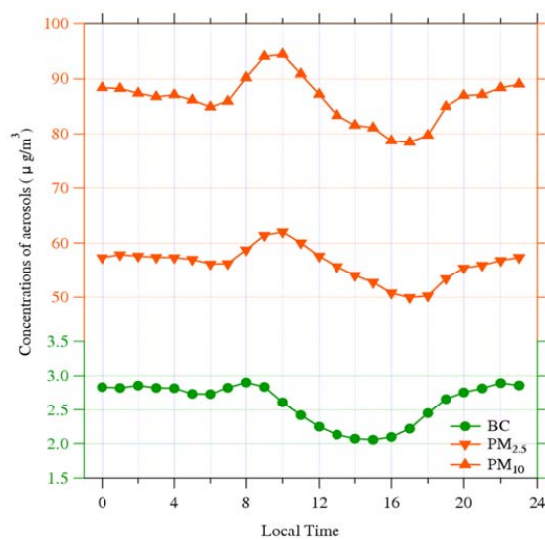
970

972 Fig 2. Seasonal variations of (a) BC, (b) PM_{2.5}, and (c) PM₁₀. Red markers represent the monthly

973

averages at Gulou site, Nanjing, China.

973



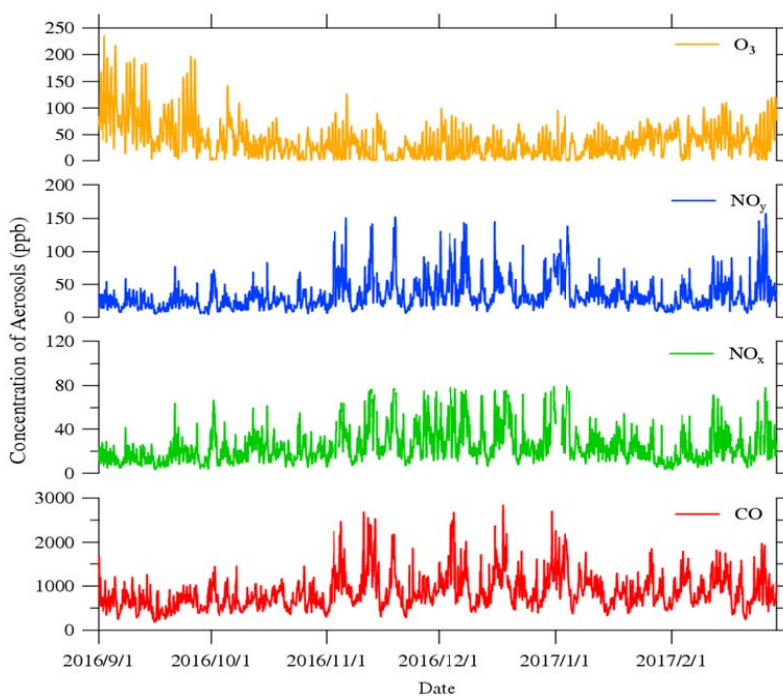
974

976 Fig 3. 6-month mean diurnal variations of BC, PM_{2.5}, and PM₁₀ at Gulou site, Nanjing, China

977

from September 2016 to February 2017.

977

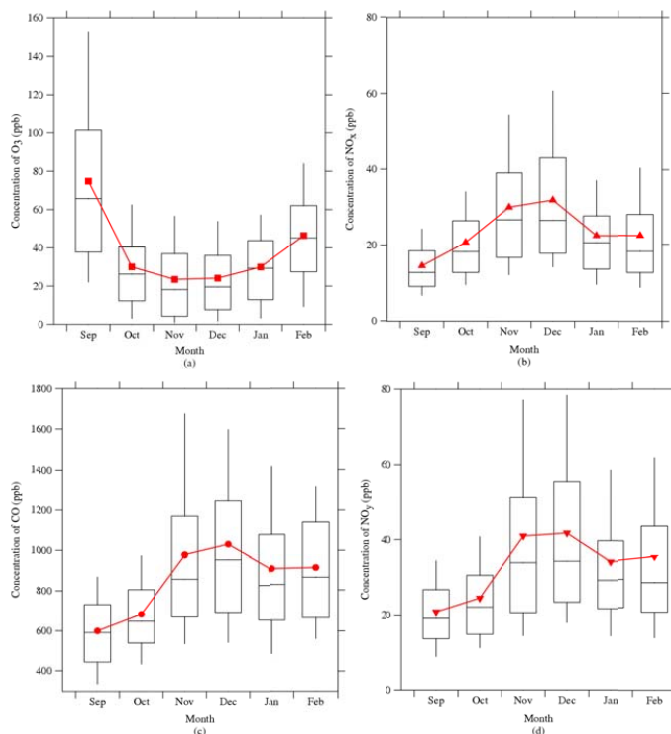


978

979

Fig.4 Time series of particles from September 2016 to February 2017 at Gulou site.

980



981

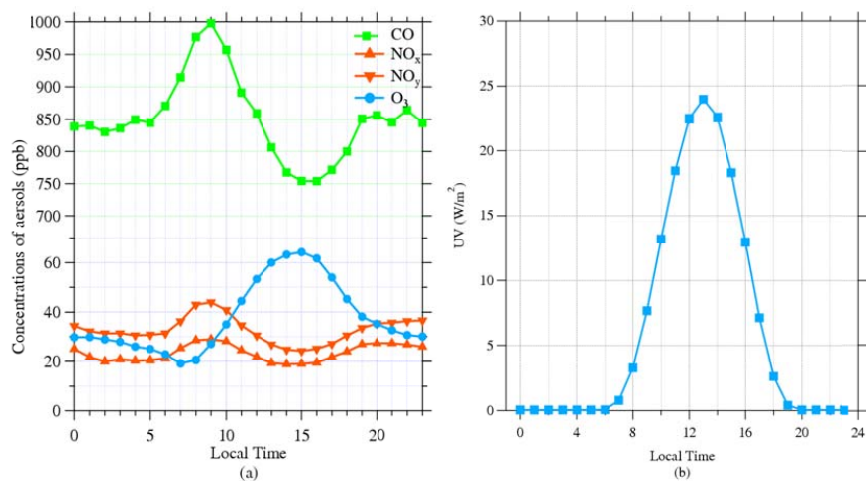
982

984 Fig 5. Seasonal variations of (a) O₃, (b) NO_x, (c) CO, and (d) NO_y. The 10, 25, 50, 75, and 90%

985 percentile values of each are shown in black, and red markers represent the monthly averages.

986

986



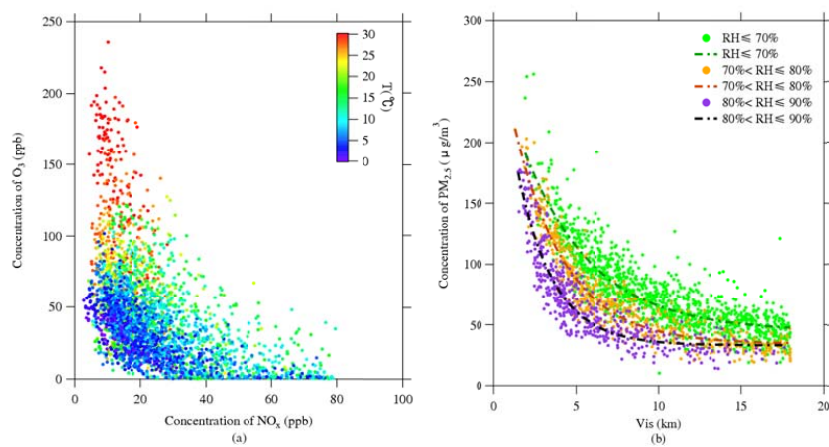
987

989 Fig 6. 6-month mean diurnal variations of (a) trace gases and (b) UV (ultra-violet radiation) at

990

Gulou site from September 2016 to February 2017

990



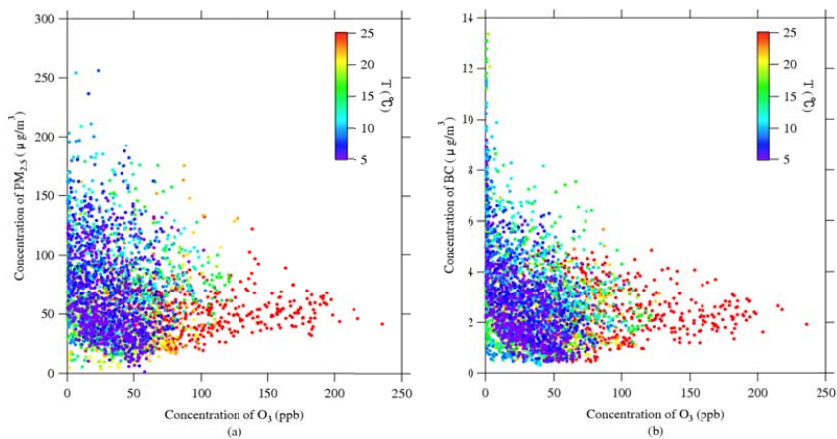
991

993

Fig 7. Scatter plots of (a) O_3 - NO_x color-coded with air temperature (T) and (b) $PM_{2.5}$ -Vis

994

color-coded with relative humidity (RH).

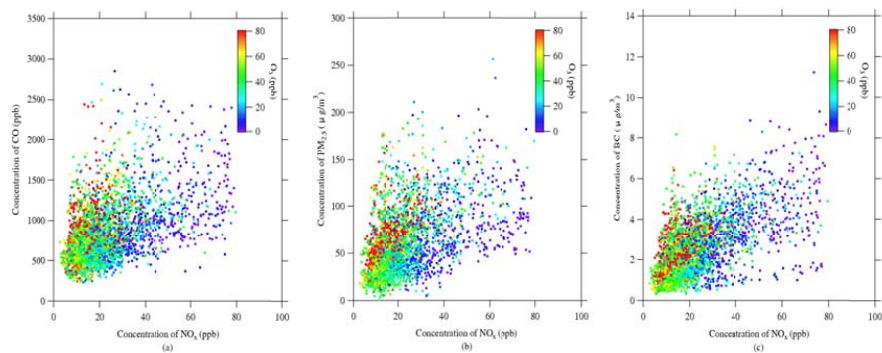


994

995

Fig 8. Scatter plots of (a) $PM_{2.5}$ - O_3 and (b) BC - O_3 color-coded with air temperature (T).

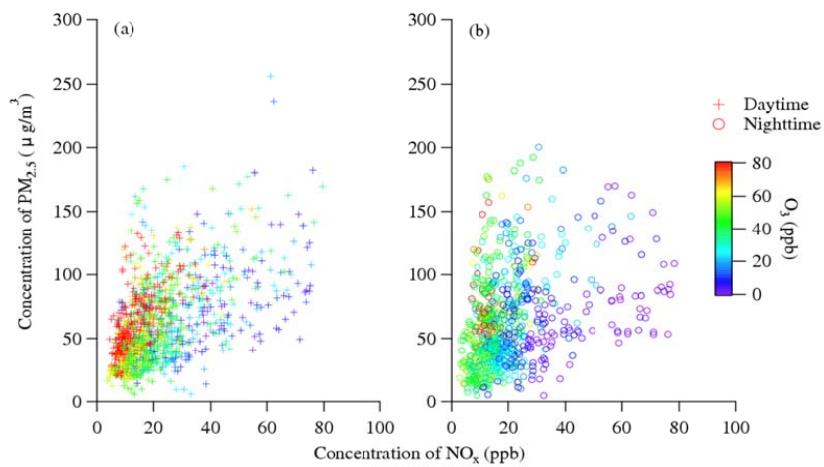
996



997

998

Fig 9. Scatter plots of (a) CO-NO_x, (b) PM_{2.5}-NO_x, and (c) BC-NO_x color-coded with O₃.

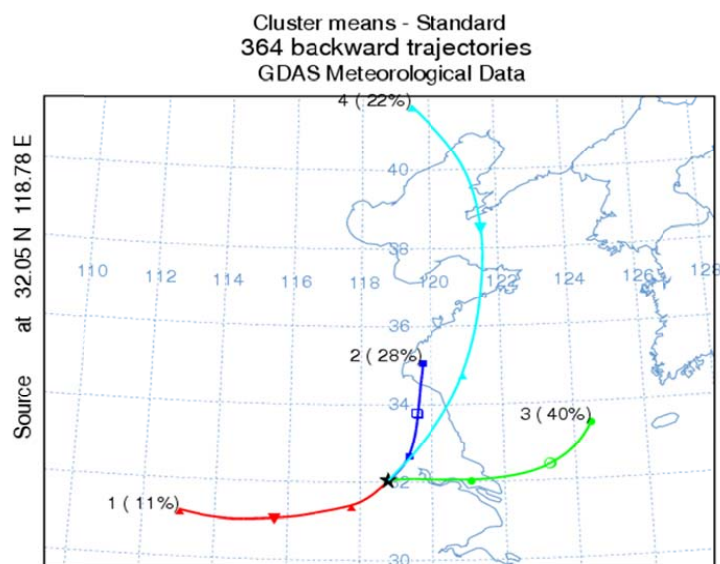


999

001 Fig 10. Scatter plots of $PM_{2.5}$ - NO_x color-coded with O_3 during (a) daytime (9:00~ 17:00) and (b)

1002

nighttime (0:00~ 6:00).



1002

1003

Fig 11. Clusters of 96 h back trajectories arriving at the study site at 100 m in 2016 fall.

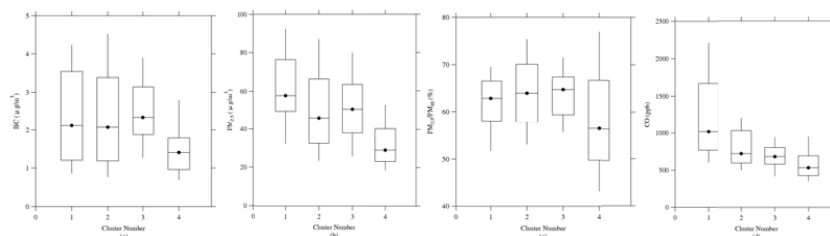
1004

1005

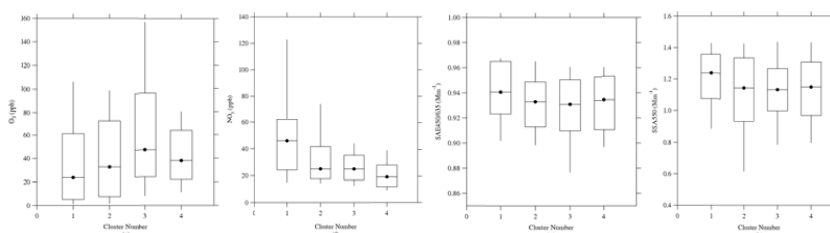
1006



1007



1008

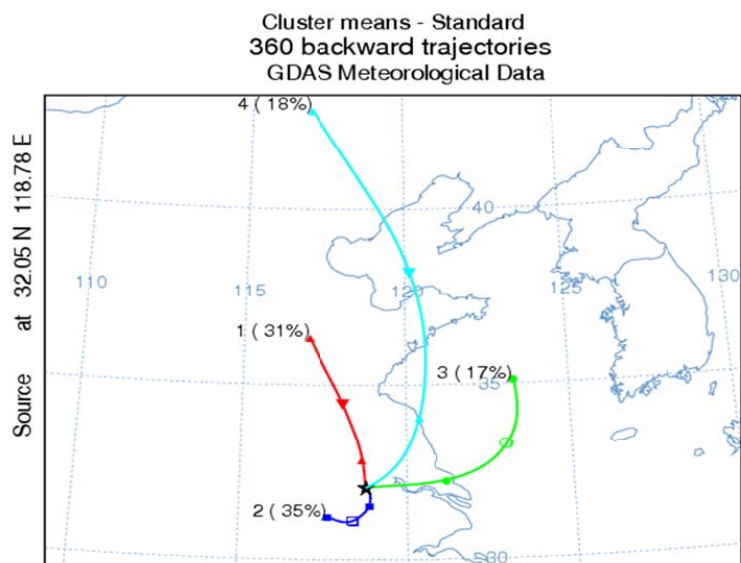


1011 Fig 12. The 10, 25, 50, 75, and 90% percentile values in each cluster of back trajectories in 2016

1012 fall of (a) BC, (b) $PM_{2.5}$, (c) $PM_{2.5}/PM_{10}$, (d) CO, (e) O_3 , (f) NO_y , (g) SAE, and (h) SSA. Black

1013 markers represent the averages.

1014

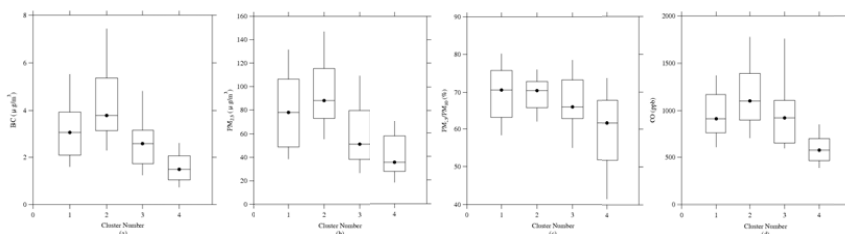


1013

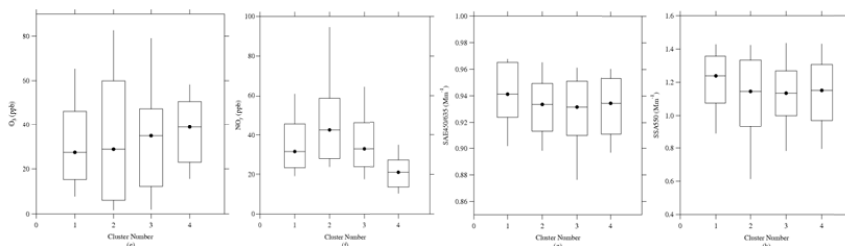
1014 Fig 13. Clusters of 96 h back trajectories arriving at the study site at 100m in 2016 winter.



1015



1016



1019

Fig 14. The 10, 25, 50, 75, and 90% percentile values in each cluster of back trajectories in 2016

1020

winter of (a) BC, (b) $\text{PM}_{2.5}$, (c) $\text{PM}_{2.5}/\text{PM}_{10}$, (d) CO, (e) O_3 , (f) NO_y , (g) SAE, and (h) SSA. Black

1021

markers represent the averages.

1020

1021

1022

1023

1024

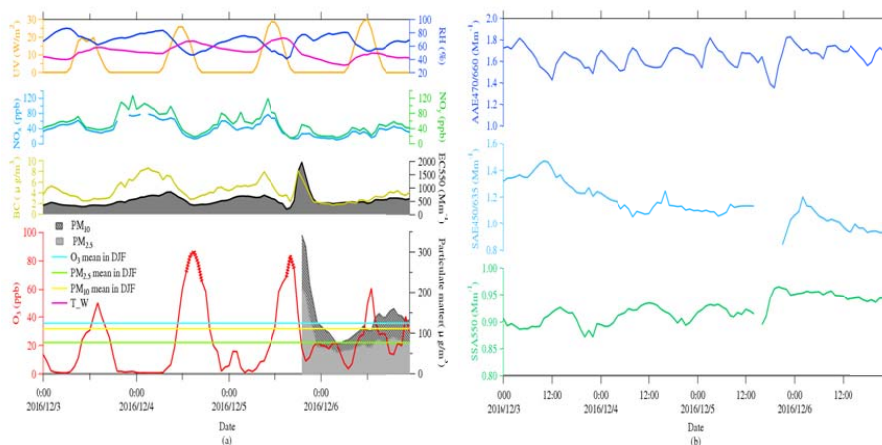
1025

1026

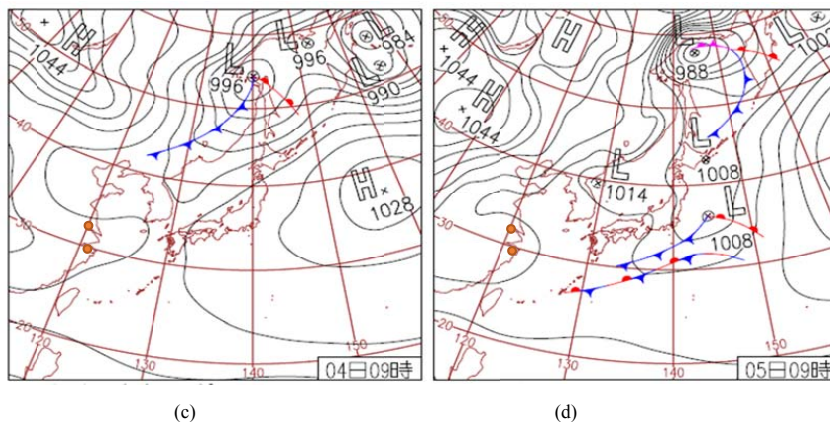
1027

1028

1029

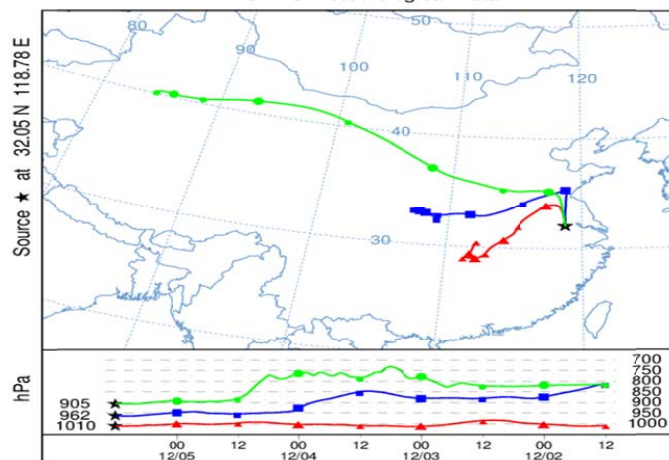


1030



1031
1032

NOAA HYSPLIT MODEL
Backward trajectories ending at 1200 UTC 05 Dec 16
GDAS Meteorological Data



1033
1034

(f)



1034 Fig 15. Time series during December 3-6, 2016, for (a) PM_{2.5}, BC and O₃ with associated
1035 meteorological parameters, trace gases and (b) optical parameters. Red markers represent O₃ over
1036 daily maximum average during winter. Weather charts on (c) 4th and (d) 5th December. (f) 96h
1037 backward trajectories analysis ending at 1200 UTC on 5th December.
1038